

Banner appropriate to article type will appear here in typeset article

# Energy-Efficient Balanced Flow Control Achieved through Optimization of Synthetic Jet Placement Based on Deep Reinforcement Learning

Wang Jia<sup>1</sup>, Hang Xu<sup>1</sup>†

<sup>1</sup>School of Ocean and Civil Engineering, Shanghai Jiao Tong University, Shanghai, 200240, China

(Received xx; revised xx; accepted xx)

This study leverages deep reinforcement learning (DRL) to train synthetic jet-based flow control strategies for circular and square cylinders. The central aim is to ascertain the optimal jet placements that strike an ideal balance between energy efficiency and control effectiveness, by formulating a cohesive strategy based on a comprehensive analysis of flow control performance and energy consumption across a range of configurations. First, the results from single-action training indicate that for circle cylinder, positioning the synthetic jet approximately  $105^\circ$  from the stagnation point achieves the most energy-efficient and effective control strategy. For square cylinder, placing the jet near the rear corner addresses the dual objectives of minimizing energy consumption and maximizing control performance. Second, compared to single-action control, multi-action control exhibits reduced convergence speed and stability. However, simultaneously activating synthetic jets at multiple locations significantly decreases initial energy consumption and enhances energy efficiency. The findings underscore the critical importance of accurately positioning the synthetic jet at the primary flow separation point, as this alignment not only enhances flow control performance but also establishes an optimal balance between energy efficiency and control effectiveness within the flow system. Furthermore, the interaction between synthetic jets and the flow system alters surface streamline patterns and local flow structures, resulting in effects that are considerably larger in scale than the jets themselves. This study crystallizes the potential of DRL algorithms to intelligently optimize intricate flow control strategies, effectively balancing energy efficiency with enhanced flow control performance through strategically optimized jet placement.

## Key words:

Authors should not enter keywords on the manuscript, as these must be chosen by the author during the online submission process.

---

**MSC Codes** (*Optional*) Please enter your MSC Codes here

† Email address for correspondence: hangxu@sjtu.edu.cn

**Abstract must not spill onto p.2**

## 1. INTRODUCTION

Active flow control (AFC) involves regulating and controlling fluid flow through external mechanisms such as injection, suction, or vibration to optimize flow characteristics and enhance system efficiency, performance, and stability. Despite significant advancements in this field over the past few decades, there remain unresolved challenges, particularly in addressing the nonlinear complexities inherent in fluid dynamics (Collis & Joslin 2004; Jahanmiri 2010). Fluid dynamics problems are intrinsically nonlinear, especially when dealing with turbulent and separated flows, where the flow behavior is extremely complex and difficult to control accurately using traditional analytical or numerical methods (Cattafesta & Sheplak 2011; Gad-el Hak 1996). The challenges are further compounded in high-dimensional and multi-scale problems, where finding a global optimum solution is particularly challenging. Consequently, there are still numerous difficulties in optimizing control strategies, achieving real-time control, enhancing system robustness, and reducing energy consumption (Bewley 2001; Brunton & Noack 2015a). Addressing these issues will not only help overcome existing technical barriers but also promote the application and development of AFC technologies in a broader range of fields (Gad-el Hak 1996; Bewley 2001; Brunton & Noack 2015b).

The rapid development of artificial intelligence brings new vitality to the field of flow control, with reinforcement learning (RL) emerging as a key machine learning algorithm that effectively addresses complex decision-making and control problems (Brunton *et al.* 2020; Ren *et al.* 2020). The core mechanism of RL lies in the agent's ability to interact with the environment, gradually optimizing its strategy based on rewards or penalties received from its actions, with the goal of maximizing cumulative rewards (Kaelbling *et al.* 1996; Sutton & Barto 2018). Reinforcement learning agents possess the ability for long-term planning and decision-making, continuously adjusting their behavior strategies in response to environmental feedback, making it a powerful tool for autonomous learning and decision-making (Arulkumaran *et al.* 2017). Deep learning (DL) has strong expressive capabilities, allowing it to approximate complex nonlinear functions (LeCun *et al.* 2015; Janiesch *et al.* 2021). When RL is combined with DL to form deep reinforcement learning (DRL), this approach leverages the feature extraction capabilities of DL and the strategy optimization strengths of RL (François-Lavet *et al.* 2018). Consequently, DRL is highly effective at tackling control challenges in high-dimensional, complex state spaces, establishing itself as a powerful technique for advancing flow control technologies and addressing intricate fluid dynamics problems.

The development of DRL traces back to the mid-20th century, with significant progress occurring as deep learning and computational power advance (Kaelbling *et al.* 1996). A pivotal milestone comes in 2013 when Google DeepMind introduces the Deep Q-Network (DQN), demonstrating DRL's remarkable potential in mastering Atari games and establishing it as a prominent and rapidly expanding research area (Mnih 2013; Arulkumaran *et al.* 2017). Subsequent advancements, particularly in proximal policy optimization (PPO) and distributed DRL techniques, further propel the field. PPO addresses the inherent instability of traditional policy gradient methods by introducing a clipped objective function, ensuring stable and efficient policy updates (Schulman *et al.* 2017). Distributed DRL, enabling parallel training across multiple machines, greatly improves computational efficiency and scalability (Sutton & Barto 2018; Liang *et al.* 2018). These developments lead to DRL applications in various domains, including AlphaGo's performance in Go, autonomous vehicle navigation, robotic operations, financial trading strategies, and smart manufacturing and healthcare (Li 2018; Silver *et al.* 2018). These applications showcase DRL's exceptional abilities in high-

dimensional perception, continuous decision-making, and complex environment handling, highlighting its immense potential and broad impact in practical applications.

Given the exceptional decision-making capabilities of reinforcement learning, its methods and derivative technologies are seeing widespread development in fluid mechanics, covering various areas such as turbulence modeling, flow prediction, shape optimization, and flow control (Rabault *et al.* 2020; Viquerat *et al.* 2022; Vignon *et al.* 2023). In the domain of turbulence modeling, Novati *et al.* (2021) leveraged multi-agent reinforcement learning to automate the discovery of turbulence models, while Kurz *et al.* (2023) utilized a multi-agent reinforcement learning framework to identify the optimal eddy viscosity model for implicitly filtered large eddy simulations. In the field of shape optimization, Viquerat *et al.* (2021) spearheaded the application of DRL for direct shape optimization, demonstrating that artificial neural networks (ANN) could autonomously generate optimal shapes within a constrained time frame and without prior knowledge, given an appropriate reward mechanism. In the context of flow control, Rabault *et al.* (2019) introduced the first application of an ANN trained via DRL for flow control, successfully reducing drag by 8%. These studies highlight the significant potential and promising prospects of DRL in the field of fluid mechanics.

AFC techniques that couple CFD with DRL have been extensively studied across various domains, including robustness across Reynolds numbers, large-scale flow separation control, parallelization strategies, algorithm comparisons, and optimization of probe distributions. Firstly, DRL controllers have shown strong generalization across various  $Re$  values. For example, Tang *et al.* (2020a) achieved significant drag and lift reduction in cylinder simulations across  $Re$  from 100 to 400, demonstrating the controllers' robustness. Wang & Xu (2024d) validated the soft actor-critic (SAC) algorithm, reducing drag by up to 47% and suppressing vortex shedding around a square cylinder across the same  $Re$  range. At  $Re = 1,000$ , Ren *et al.* (2021) applied DRL to active flow control, achieving a 30% drag reduction under weak turbulence. Furthering this, Wang *et al.* (2024) introduced a self-learning algorithm, enhancing DRL to achieve drag reductions of 32.2% at  $Re = 500$ , 46.55% at  $Re = 1,000$ , and 28.6% in 3D turbulence at  $Re = 10,000$ .

Secondly, DRL algorithms have been effectively applied to control complex flow separation phenomena around a wide range of geometries, demonstrating their versatility and robustness. These applications include fluidic pinball systems (Feng *et al.* 2023), square cylinder (Wang & Xu 2024d), airfoil (Wang *et al.* 2022b), elliptical cylinder (Wang & Xu 2024a), and flat plate (Wang & Xu 2024a). For instance, Feng *et al.* (2023) demonstrated that DRL could achieve effective control in fluidic pinball systems, delivering results that were comparable to, and in some cases even surpassed, optimal strategies developed through conventional methods. In another study, Wang & Xu (2024a) applied DRL to active flow control on elliptical cylinders with varying aspect ratios, successfully reducing drag and suppressing vortex shedding. However, they noted that as the aspect ratio decreases, the control challenges increase accordingly. These studies show DRL's wide applicability and effectiveness in optimizing bluff body flow performance.

Thirdly, significant progress has been made in refining DRL algorithms and optimizing probe placements. Li & Zhang (2022) found that positioning probes in sensitive regions enhances control efficiency, even with fewer probes. Xia *et al.* (2024) promoted an energy-efficient reinforcement learning approach for drag reduction using partial surface pressure measurements, while Suárez *et al.* (2024) demonstrated an 8% drag reduction in 3D turbulent flow with DRL-based AFC strategies, achieving better mass cost efficiency than traditional controls. Additionally, Paris *et al.* (2021a) developed a sensor optimization algorithm that reduced the number of sensors while maintaining high performance. Parallelization has also proven crucial for DRL in flow control. Rabault & Kuhnle (2019) showed that parallelizing simulations accelerates the discovery of control strategies. Wang *et al.* (2022a) developed

*DRLinFluids*, integrating DRL with OpenFOAM to support further research. Wang & Xu (2024c) improved parallel efficiency, achieving a 47-fold increase in training speed.

Although previous studies have explored DRL-based AFC from multiple perspectives, we found that the placement of jet actuators significantly impacts control effectiveness and energy consumption. Recent research has begun to examine how the position of synthetic jets affects control performance. Chen *et al.* (2023) studied DRL-based AFC to mitigate vortex shedding in a square cylinder at  $Re = 100$ , finding that jet actuators placed near the rear corners provided the best control performance. Yan *et al.* (2023) investigated the effects of symmetrically deploying jet actuators at the front and rear corners of a square cylinder at  $Re = 500, 1,000, \text{ and } 2,000$ . The study found that placing the actuators near the front corners resulted in superior control performance. Wang & Xu (2024b) used a DRL algorithm to control the mass flow rate of synthetic jets on the top and bottom surfaces of a square cylinder at  $Re = 100 \text{ and } 500$ , achieving active flow control and analyzing the sensitivity of performance to jet position and width. Yan *et al.* (2024) studied lift and drag control in rectangular cylinders at  $Re = 1,000$  across four aspect ratios, finding that a configuration with eight DRL-controlled actuators at the corners performed best.

Building on the aforementioned research, we have recognized that the placement of synthetic jets plays a crucial role in determining flow control performance. Moreover, we have observed that many studies lack a thorough evaluation of control costs when assessing flow control effectiveness. For active flow control strategies to be viable, they must achieve the desired outcomes while also ensuring energy efficiency. This necessitates that the control strategy optimizes flow behavior with minimal energy input, thereby avoiding excessive energy consumption due to the control measures themselves. Additionally, the variability of optimal jet positions across different Reynolds numbers has captured our attention. We propose that a fluid dynamics-based analysis could provide unified guidelines for the strategic placement of synthetic jets. To this end, we plan to investigate the placement of synthetic jets for flow control around both square and circular cylinder at  $Re = 100$ .

This study will consider multiple situations, including single-agent control of individual jet pairs, single-agent simultaneous control of multiple jet pairs, and the development of distinct control strategies for each jet pair. Through these configurations, we aim to optimize both control performance and energy efficiency. Crucially, a physical analysis of the training results for flow around circular and square cylinders offers qualitative insights into the design of jet positioning. This analysis is expected to yield a deeper understanding of the underlying physical principles that govern the effectiveness of different jet locations in managing separated flows. The structure of this paper is as follows: § 2 describes the research problem and the framework for coupling DRL with AFC. § 3 and § 4 present the results of the DRL training. In § 5, we analyze and discuss the physical phenomena observed in the training results for both circular and square cylinder flows. Finally, § 6 summarizes the conclusions of this study.

## 2. METHODOLOGY

We use DRL algorithms to manipulate synthetic jets for active flow control, focusing on the impact of jet positioning on flow performance around square and circular cylinders at  $Re = 100$ . The fundamental numerical methods, software, and key parameters are outlined in § 2.1. In § 2.2, we describe the flow characteristics around a circular cylinder and the arrangement of the synthetic jets, while § 2.3 provides corresponding details for a square cylinder. § 2.4 introduces the core concepts, mathematical models, and distinctions of deep learning and reinforcement learning, with a detailed discussion of the PPO algorithm. Lastly, § 2.5 demonstrates the application of DRL algorithms to address flow control challenges,

offering a comprehensive overview of the agent-environment framework and related key concepts.

### 2.1. Numerical simulation

We describe the behavior of incompressible viscous fluid flow within the domain  $\Omega \subset \mathbb{R}^{nd}$  over the time interval  $(0, T)$  using the Navier-Stokes equations. These equations govern the evolution of the fluid velocity field  $\mathbf{u} = \mathbf{u}(\mathbf{x}, t)$  and pressure field  $p = p(\mathbf{x}, t)$ , where  $\mathbf{x}$  represents the spatial coordinates and  $t$  denotes time. The governing equations in their non-dimensional form are expressed as:

$$\frac{\partial \mathbf{u}}{\partial t} + \mathbf{u} \cdot (\nabla \mathbf{u}) = -\nabla p + Re^{-1} \Delta \mathbf{u} \quad \text{in } \Omega \times (0, T), \quad (2.1a)$$

$$\nabla \cdot \mathbf{u} = 0 \quad \text{in } \Omega \times (0, T), \quad (2.1b)$$

where  $\mathbf{u}$  denotes the non-dimensional velocity,  $t$  represents the non-dimensional time, and  $p$  is the non-dimensional pressure. The Reynolds number is defined as  $Re = \frac{UD}{\nu}$ , where  $\nu$  denotes the kinematic viscosity of the fluid.

This study employs `OpenFOAM` for numerical simulations, a widely used and flexible Navier-Stokes solver that is highly regarded in both industry and academia (Jasak *et al.* 2007). In the process of solving partial differential equations using the finite volume method, we divide the computational domain into a finite number of control volumes to more accurately capture and analyze the complex behavior of fluids. The `pimpleFoam` solver is specifically designed for addressing unsteady Navier-Stokes equations. It integrates the Semi-Implicit Method for Pressure-Linked Equations (SIMPLE) with the Pressure-Implicit with Splitting of Operators (PISO) algorithms (Issa 1986; Jang *et al.* 1986). This integration enables the effective resolution of complex, time-dependent flow scenarios, allowing for larger time steps while maintaining both stability and computational efficiency.

### 2.2. Circular cylinder environment

The configuration employed in this study for simulating flow around a circular cylinder closely follows the classical benchmark established by Schäfer *et al.* As illustrated in figure 1, the cylinder is placed within a rectangular computational domain with dimensions of  $22D$  along the  $x$ -axis and  $4.1D$  along the  $y$ -axis. The origin of the Cartesian coordinate system is positioned at the center of the cylinder. The cylinder is slightly offset in the  $y$ -direction to induce vortex shedding, facilitating the analysis of oscillatory flow phenomena. The boundaries of the computational domain are divided into an inlet  $\Gamma_{\text{in}}$ , an outlet  $\Gamma_{\text{out}}$ , no-slip walls  $\Gamma_w$ , and two separate jets on the cylinder  $\Gamma_i$  ( $i = 1, 2$ ), as shown in figure 1(a). At the inlet  $\Gamma_{\text{in}}$ , the inflow velocity along  $x$ -axis is prescribed by a parabolic velocity profile in the form,

$$U_{\text{inlet}}(y) = U_m \frac{(H - 2y)(H + 2y)}{H^2}, \quad (2.2)$$

and that along  $y$ -axis is prescribed as,

$$V_{\text{inlet}}(y) = 0. \quad (2.3)$$

$U_m$  is the maximum velocity magnitude of the parabolic profile, and  $H = 4.1D$  represents the total height of the rectangular domain. The average inlet velocity  $\bar{U}$ , is related to the parabolic velocity profile  $U_{\text{inlet}}(y)$  through the expression:

$$\bar{U} = \frac{1}{H} \int_{-H/2}^{H/2} U_{\text{inlet}}(y) dy = \frac{2}{3} U_m. \quad (2.4)$$

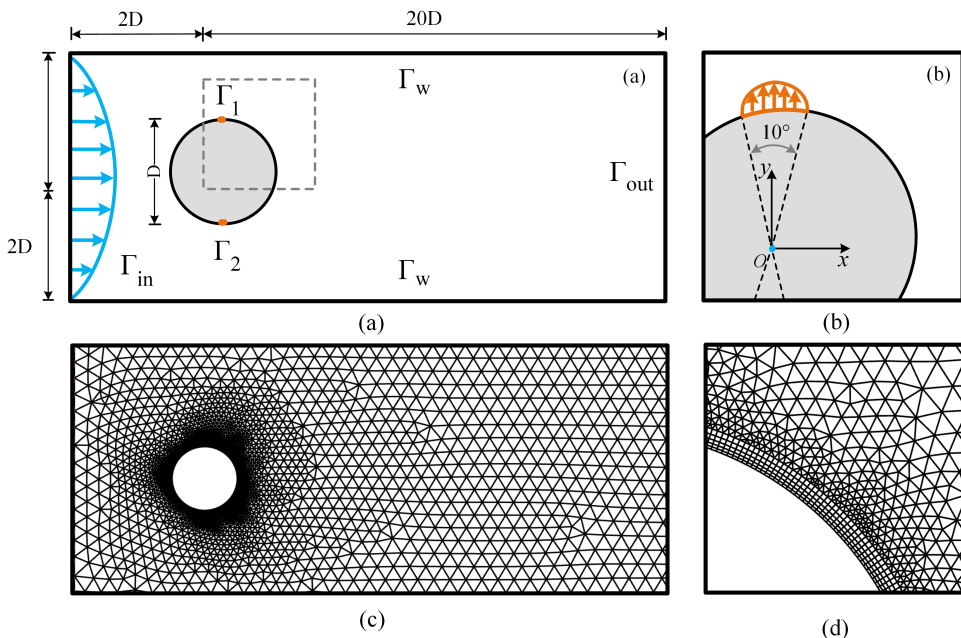


Figure 1: Numerical simulation model of flow around a cylinder. (a) Domain configuration and boundary conditions. (b) Details of the jets conditions on the cylinder. Jets are located at  $\Omega = 90^\circ$  and  $\Omega = 270^\circ$  on the cylinder, with a jet width of  $\omega = 10^\circ$ . Parabolic velocity distribution is used for each jet. (c) Mesh structure around the object, and (d) Zoomed-in view of the mesh near the cylinder boundary.

Flow control on the cylinder surface is achieved by introducing synthetic jets at the top and bottom points, as shown in figure 1(b). These jets, denoted as  $\Gamma_i$  ( $i = 1, 2$ ), can inject or suction fluid to control the flow around the cylinder. Each jet spans an angular width of  $\omega = 10^\circ$  and is oriented perpendicularly to the outer surface of the cylinder. The velocity profile within each jet follows a parabolic distribution, allowing for both positive (blowing) and negative (suction) velocities. A key aspect of the AFC implementation is ensuring mass conservation within the system. This is achieved by balancing the net mass flow rates of the jets, i.e.,  $V_{\Gamma_1} = -V_{\Gamma_2}$ , which ensures that the net flow into or out of the system remains zero.

Additionally, a no-slip boundary condition is enforced on the areas of the cylinder surface where the jets are not located, preventing any relative motion between the fluid and the cylinder in those regions. At the outlet boundary  $\Gamma_{out}$ , an outflow condition is applied, where the velocity is extrapolated based on the internal flow field. No-slip boundary conditions are also applied at the upper and lower walls  $\Gamma_w$ , ensuring that the velocity at these walls is zero relative to the boundary surface. This specification of boundary conditions ensures accurate flow simulation and effective control through synthetic jets. Mathematically, the boundary conditions are written as:

$$\begin{aligned}
 -\rho \mathbf{n} \cdot \mathbf{p} + Re^{-1}(\mathbf{n} \cdot \nabla \mathbf{u}) &= 0 & \text{on } \Gamma_{out}, \\
 \mathbf{u} &= 0 & \text{on } \Gamma_w, \\
 \mathbf{u} &= U & \text{on } \Gamma_{in}, \\
 \mathbf{u} &= f_{Q_i} & \text{on } \Gamma_i, \quad i = 1, 2.
 \end{aligned} \tag{2.5}$$

where,  $\mathbf{n}$  denotes the normal vector,  $U$  is the inflow velocity, and  $f_{Q_i}$  represents the radial velocity profiles simulating the suction or injection of fluid by the jets.

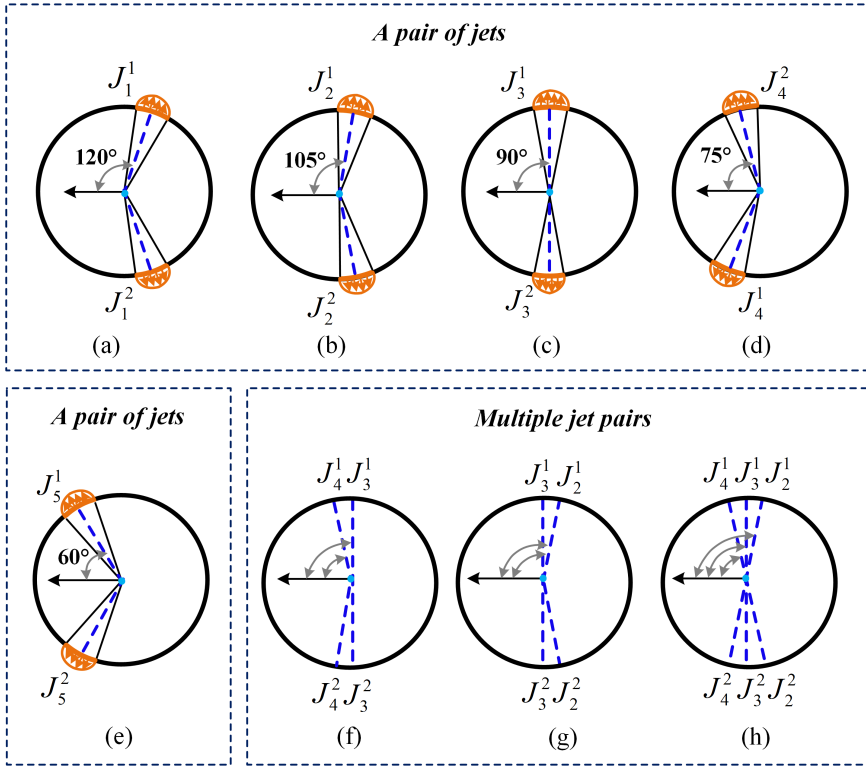


Figure 2: For a single pair of jets, five different arrangements are considered: (a)  $J_1^1$  and  $J_1^2$ , (b)  $J_2^1$  and  $J_2^2$ , (c)  $J_3^1$  and  $J_3^2$ , (d)  $J_4^1$  and  $J_4^2$ , (e)  $J_5^1$  and  $J_5^2$ . For two pairs of jets, two arrangements are examined: (f)  $J_3^1, J_3^2, J_4^1$ , and  $J_4^2$ ; (g)  $J_3^1, J_3^2, J_2^1$ , and  $J_2^2$ . For three pairs of jets, one arrangement is studied: (h)  $J_2^1, J_2^2, J_3^1, J_3^2, J_4^1$ , and  $J_4^2$ .

To thoroughly investigate the impact of synthetic jets positioning on flow control performance around a circular cylinder, a series of experiments is conducted, employing various jet configurations: one pair, two pairs, and three pairs of jets. In the single-pair configuration, five different jet placement schemes are examined to evaluate their effectiveness in controlling the flow. Each scheme is designated according to the position of the jets. For example,  $J_1^1$  and  $J_1^2$  refer to a pair of synthetic jets symmetrically positioned about the  $x$ -axis, with a net mass flow rate of zero across the pair. In the notation  $J_1^1$ , the subscript 1 indicates the first pair of synthetic jets, while the superscript 1 designates the first jet within that pair.

For each jet placement scheme, the azimuthal angles of the first jet in each pair are indicated in the figures. The configurations considered in this study include jets positioned at angles of  $60^\circ$ ,  $75^\circ$ ,  $90^\circ$ ,  $105^\circ$ , and  $120^\circ$ . For the two-pair configuration, we explore two different placement schemes to evaluate the interaction effects between multiple pairs of jets. The three-pair configuration involves a specific arrangement designed to provide deeper insights into the cumulative effects of additional jet pairs on flow control. In this configuration, flow control is achieved by simultaneously activating  $J_2^1, J_2^2, J_3^1, J_3^2, J_4^1$ , and  $J_4^2$ . The precise locations and nomenclature of these jets are detailed in figure 2.

In scenarios involving multiple jet pairs, it is important to emphasize that the control strategy derived from DRL assigns distinct actions to each individual pair of jets. This approach allows the agent to assign distinct action values to jets positioned at various

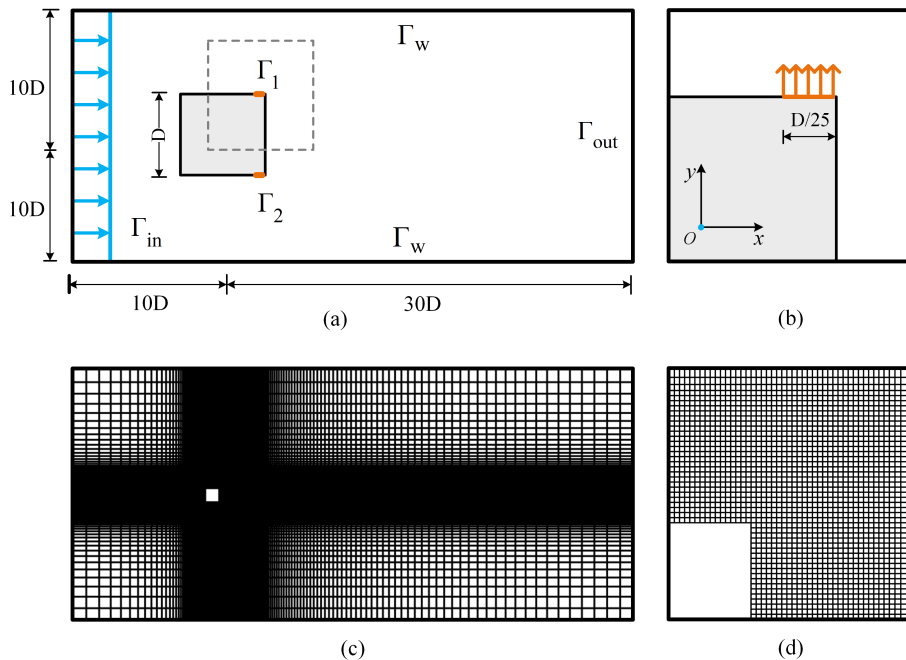


Figure 3: Schematic of the computational domain and boundary conditions. (a) Establishment of the coordinate system and detailed dimensions of the computational domain. (b) Placement of the synthetic jets near the trailing corner point. (c) The mesh generation scheme around the square object, illustrating the distribution of high-density mesh in regions prone to flow separation, and (d) A close-up view of the mesh structure, highlighting the refinement near the boundary layer.

locations, facilitating tailored control that considers the unique dynamics associated with each jet placement. By assigning unique actions to each jet pair, the DRL framework facilitates the evaluation of the relative effectiveness of flow control at different positions. This method enables the quantification of the contribution of each jet pair to the overall control strategy, providing a deeper understanding of the role each jet plays in modulating the flow dynamics.

The objective of this study is to develop a DRL-based control strategy that enables simultaneous flow control at multiple positions on the cylinder. By assigning distinct actions to each individual jet pair, the agent can tailor the control to the specific dynamics associated with the placement of each jet. This approach allows for a systematic comparison of jet performance at various locations, facilitating the evaluation of the relative effectiveness of flow control across different positions. Furthermore, this comparison is complemented by an analysis of the underlying causes of observed performance differences, informed by principles of fluid mechanics. Such a comprehensive analysis enhances our understanding of how the contribution of each jet is influenced by its position and the physical mechanisms governing the flow dynamics.

### 2.3. Square cylinder environment

The computational domain for simulating the flow around a square cylinder is precisely defined with dimensions of  $40D \times 20D$ , where  $D$  represents the characteristic side length of the cylinder. The origin is located at the center of the cylinder, with  $10D$  extending both above and below this point to define the vertical boundaries. The domain extends  $10D$  upstream from the cylinder to the inlet boundary  $\Gamma_{in}$ , providing sufficient distance for the



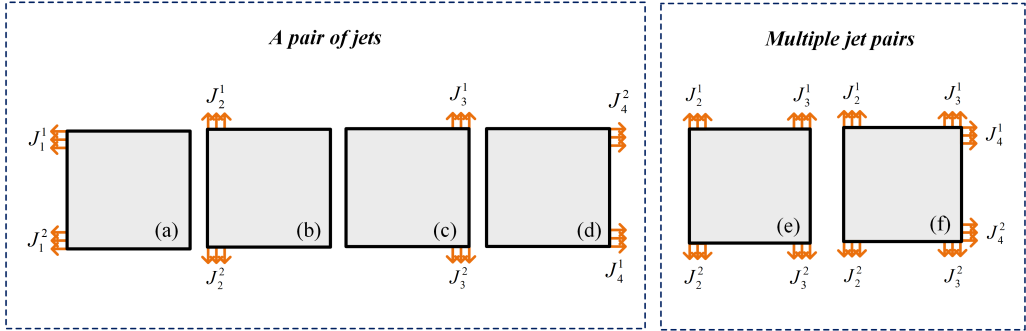


Figure 4: Jets arrangement schemes for the flow around a square cylinder. For a single pair of jets, five different arrangements are considered: (a)  $J_1^1$  and  $J_2^1$ ; (b)  $J_2^1$  and  $J_2^2$ ; (c)  $J_3^1$  and  $J_3^2$ ; (d)  $J_4^1$  and  $J_4^2$ . For two pairs of jets, two arrangements are examined: (e)  $J_2^1$ ,  $J_2^2$ ,  $J_3^1$  and  $J_3^2$ ; For three pairs of jets, one arrangement is studied: (f)  $J_2^1$ ,  $J_2^2$ ,  $J_3^1$ ,  $J_3^2$ ,  $J_4^1$  and  $J_4^2$ .

flow to fully develop into a uniform profile before interacting with the cylinder. Downstream, the domain stretches  $30D$  from the cylinder to the outlet boundary  $\Gamma_{\text{out}}$ , ensuring ample space for capturing the wake formation and vortex shedding phenomena. As illustrated in figure 3(a), this spatial configuration is carefully optimized to minimize the influence of boundary effects on the flow around the cylinder while ensuring that the downstream region is sufficiently extended to capture the wake dynamics with high accuracy. This design is critical for maintaining the fidelity of the numerical simulations and ensuring the robustness and reliability of the results.

In the simulation setup, the inlet of the computational domain is prescribed with a uniform velocity profile, where the velocity magnitude is set to 2 and aligned along the  $x$ -axis. The synthetic jets are configured with velocities perpendicular to the walls of the square cylinder, directed along the outward normal to these walls, as illustrated in figure 3(b). Except at the locations of the synthetic jets, the remaining sections of the square cylinder walls are subjected to no-slip solid wall boundary conditions, ensuring that the fluid adheres to the surfaces and accurately reflecting the physical constraints imposed by solid boundaries on the fluid flow. At the outlet boundary, Neumann-type conditions are applied to maintain a zero stress vector, effectively simulating the natural flow behavior at an infinite distance. The upper and lower boundaries of the domain are defined with far-field boundary conditions, designed to minimize their impact on the flow around the square cylinder and closely approximate an unbounded fluid domain. This careful configuration ensures the accuracy and reliability of the simulation, allowing for a precise investigation of the flow dynamics.

To ensure numerical stability, the time step size is carefully selected as  $\Delta t = 0.0005$  following extensive validation and iterative testing. This choice balances temporal accuracy with adherence to the CFL condition, particularly in regions of high flow velocity and steep gradients. The rigorous selection of this parameter minimizes numerical errors, thereby enhancing the fidelity of the simulation and ensuring a reliable analysis of the fluid dynamics. The mesh topology surrounding the square cylinder is illustrated in figure 3(c). The global mesh is designed to systematically coarsen with increasing radial distance from the cylinder, optimizing computational efficiency while maintaining accuracy. In contrast, figure 3(d) highlights the local mesh refinement near the cylinder, where the grid undergoes significant densification to form high-resolution elements. This local refinement is essential for accurately capturing the intricate flow dynamics within the boundary layer, particularly in areas with elevated shear and steep velocity gradients. Such precision in mesh design

is crucial for resolving critical flow phenomena and ensuring the overall reliability of the simulation results.

To investigate the impact of synthetic jets positioning on the flow control performance around a square cylinder, we design a series of experiments with different jet configurations: one pair of jets, two pairs of jets, and three pairs of jets. In the one-pair jet configuration, we explore four different jet placement schemes. Each scheme involves a distinct spatial arrangement to assess the optimal positioning for effective flow control. The four different jet placement schemes are named according to the location of the synthetic jets. For instance,  $J_1^1$  and  $J_1^2$  represent a pair of jets located near the front corners of the square cylinder, where the subscript "1" indicates the first pair of synthetic jets, which has a net mass flow rate of zero. The superscript "1" or "2" distinguishes between the two different jets within the pair.

For the two-pair jet configuration, we investigate a single jet placement scheme aimed at analyzing how two strategically positioned pairs of jets influence the flow dynamics. Similarly, for the three-pair jet configuration, we examine a specific jet placement scheme to understand the effects of three pairs of jets on flow control performance. The precise positions and designations of the jets for each configuration are detailed in figure 4. Notably, in scenarios involving multiple pairs of jets, the control strategy derived from DRL provides distinct control actions for each individual pair of jets. This approach allows for a nuanced assessment of how different configurations and placements of synthetic jets influence the overall control effectiveness in modifying the flow around the square cylinder.

## 2.4. Deep Reinforcement Learning

Deep learning is a critical branch of machine learning, with its core centered on utilizing the multi-layered structure of artificial neural networks to process and analyze data. This multi-layered structure, also known as deep neural network, consists of an input layer, multiple hidden layers, and an output layer (LeCun *et al.* 2015). The input layer receives raw data, such as image pixels or text word vectors, and introduces these features into the network. The hidden layers, positioned between the input and output layers, are composed of interconnected neurons and are responsible for the layer-by-layer processing and transmission of information. The output layer generates the final prediction results or classification labels, with its structure and the number of neurons tailored to the specific task (Granter *et al.* 2017). Through this layered processing and non-linear transformations, DNN can automatically extract complex features from raw data and capture intricate patterns, enabling deep learning to exhibit exceptional performance in tasks such as image recognition, natural language processing, and speech recognition.

Reinforcement Learning is a sophisticated machine learning paradigm that emphasizes empowering an agent to autonomously learn optimal actions within a dynamic environment through a process of trial and error (Mnih 2013). The objective of the agent is to maximize cumulative rewards over time by continuously interacting with the environment, receiving feedback in the form of rewards or penalties, and incrementally refining the strategy to make increasingly effective decisions (François-Lavet *et al.* 2018; Wang *et al.* 2020). Through this iterative process, the agent adapts to the complexities of the environment and discovers the most advantageous actions to achieve long-term goals, ultimately enhancing its ability to make informed and efficient decisions across a wide range of scenarios.

### 2.4.1. Foundation

The agent is the entity that executes actions, learning and optimizing its strategy through repeated interactions with the environment, as depicted in figure 5(a), which illustrates the basic structure of agent-environment interaction. The environment serves as the external system within which the agent operates, providing feedback in the form of rewards based

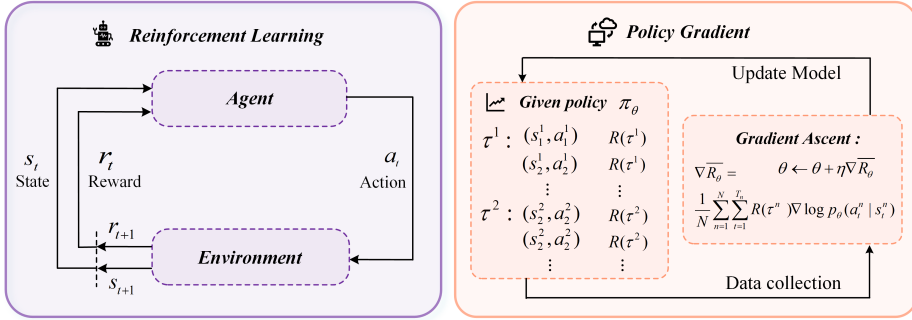


Figure 5: Basic structures of (a) Reinforcement Learning and (b) Policy gradient.

on the actions taken by the agent ( $a \in \mathbb{A}$ ) (François-Lavet *et al.* 2018). The state ( $s \in \mathbb{S}$ ) represents a snapshot of the environment at a specific moment, typically perceived by the agent as information from the environment. The agent uses a policy ( $\pi(a|s)$ ), which is a set of rules or a function that guides the selection of actions based on the current state. The policy can be either deterministic or stochastic. The state value function ( $V(s)$ ) evaluates the desirability of a particular state, representing the expected cumulative reward that can be obtained starting from that state. Similarly, the action value function ( $Q(s, a)$ ) assesses the desirability of taking a specific action in a given state, representing the expected cumulative reward that can be achieved by executing that action in the state (Wang *et al.* 2020).

#### 2.4.2. Mathematical model

RL fundamentally relies on the concept of a finite markov decision process (MDP) to model the decision-making process (Puterman 1990; Altman 1999). A finite MDP is characterized by the tuple  $(S, A, P, R, \gamma)$ , where  $S$  represents the finite state space,  $A$  denotes the finite action space,  $P$  is the state transition probability function, and  $R$  is the reward function. The discount factor  $\gamma$  quantifies the relative importance of future rewards compared to immediate rewards (Puterman 1990). At each time step  $i$ , the agent observes the environment in state  $s_i$ , selects an action  $a_i$ , and transitions to the next state  $s_{i+1}$  with probability  $p(s_{i+1}|s_i, a_i)$ . The agent then receives a reward  $R(s_i, a_i, s_{i+1})$  associated with this transition. The decision-making process is governed by a policy  $\pi(a_i|s_i)$ , which specifies the probability of choosing action  $a_i$  given the current state  $s_i$  (Altman 1999).

#### 2.4.3. Classification

RL can be broadly categorized into two main types: value-based methods and policy-based methods. Value-based methods involve learning a  $V(s)$  or a  $Q(s, a)$  that estimates the expected cumulative reward for a given state or state-action pair (Li 2018; Altman 1999). The agent selects the optimal action by maximizing these value functions, with examples including Q-learning and DQN (Mnih *et al.* 2015). Policy-based methods, on the other hand, directly learn a policy function ( $\pi(a|s)$ ), which represents the probability distribution of selecting actions given a particular state (Li 2018; Kaiser *et al.* 2024). The agent optimizes the policy function to maximize cumulative rewards, making this approach effective in handling continuous action spaces and stochastic policies. Common policy-based algorithms include policy gradient methods (Silver *et al.* 2014), trust region policy optimization (TRPO) (Schulman *et al.* 2015), and PPO (Schulman *et al.* 2017). The basic training structure of policy-based algorithms is illustrated in figure 5(b).

DNNs are a class of machine learning models composed of multiple layers of interconnected neurons, capable of automatically learning and extracting features from data (LeCun

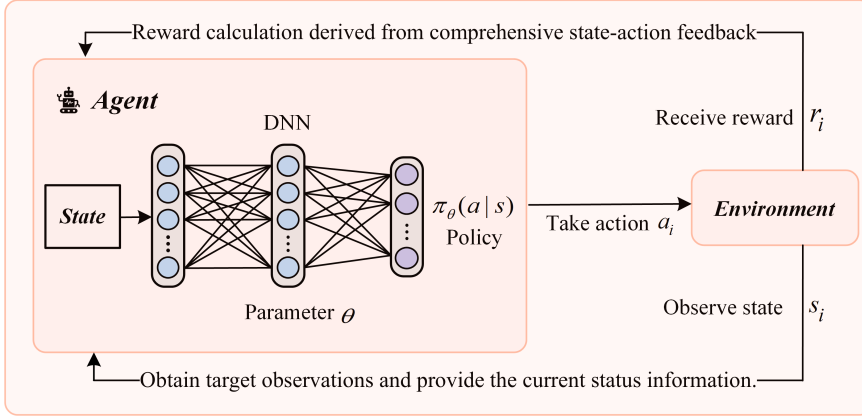


Figure 6: Basic structures of deep reinforcement learning.

*et al.* 2015). They excel in handling complex, high-dimensional datasets, making them essential for tasks such as image recognition, natural language processing, and reinforcement learning. In the framework of DRL, where DL plays a central role, the combined operation of DL and RL is depicted in figure 6. By using DNNs, deep learning can automatically extract key features from complex and high-dimensional data, significantly enhancing the ability of reinforcement learning to deal with complex environments. The functional representation ability of deep learning is extremely powerful, especially in policy representation and value function approximation, where it plays a crucial role. These capabilities enable DRL to achieve more accurate and efficient decision-making in high-dimensional, continuous action spaces, greatly improving its application effect and breadth in complex decision-making environments (Arulkumaran *et al.* 2017).

In reinforcement learning, the  $V(s)$  and the  $Q(s, a)$  are used to evaluate the goodness of a state or a state-action pair, typically represented in terms of cumulative rewards. The  $V(s)$  represents the expected cumulative reward that can be obtained starting from state  $s$  and following a policy  $\pi$  (Szepesvári & Littman 1999). It is defined as:

$$V(s) = \mathbb{E}_{\pi} \left[ \sum_{t=0}^{\infty} \gamma^t r_t \mid s_0 = s \right], \quad (2.6)$$

where  $\mathbb{E}_{\pi}$  denotes the expectation under the policy  $\pi$ .  $\gamma$  is the discount factor,  $0 \leq \gamma \leq 1$ , which discounts future rewards.  $r_t$  is the immediate reward received at time step  $t$ .  $s_0 = s$  indicates that the initial state is  $s$ .

The action value function  $Q(s, a)$  represents the expected cumulative reward that can be obtained by taking action  $a$  in state  $s$  and subsequently following the policy  $\pi$ . It is defined as:

$$Q(s, a) = \mathbb{E}_{\pi} \left[ \sum_{t=0}^{\infty} \gamma^t r_t \mid s_0 = s, a_0 = a \right], \quad (2.7)$$

where  $\mathbb{E}_{\pi}$  similarly denotes the expectation under the policy  $\pi$ .  $\gamma$  is the discount factor.  $r_t$  is the immediate reward received at time step  $t$ .  $s_0 = s$  indicates that the initial state is  $s$ , and  $a_0 = a$  indicates that the initial action is  $a$ . These two functions together describe the expected cumulative rewards associated with different states and state-action pairs, helping the agent optimize its policy to maximize long-term returns.

The advantage function  $A(s, a)$  is typically computed based on the  $V(s)$  and the  $Q(s, a)$ .

The advantage function  $A(s, a)$  evaluates the relative benefit of taking action  $a$  in a given state  $s$  compared to other possible actions (Henderson *et al.* 2018). The standard formula is:

$$A(s, a) = Q(s, a) - V(s), \quad (2.8)$$

where  $Q(s, a)$  is the action value function, representing the expected cumulative reward for taking action  $a$  in state  $s$ .  $V(s)$  is the state value function, representing the expected cumulative reward for being in state  $s$  without considering which action is taken.

PPO is a powerful policy optimization algorithm that maintains the stability of policy performance by limiting the amplitude of policy updates. It uses a proxy objective function to encourage policy updates so that the probability ratio of the current policy to the old policy remains within a certain range, thereby avoiding drastic fluctuations in policy performance. Also, PPO uses the advantage function to evaluate the advantage of state-action pairs, and optimizes the proxy objective function through stochastic gradient descent, ultimately finding the optimal policy that can obtain the highest expected cumulative reward (Schulman *et al.* 2017).

$$L^{\text{CLIP}}(\theta) = \hat{\mathbb{E}}_t \left[ \min \left( \frac{\pi_\theta(a_t|s_t)}{\pi_{\theta_{\text{old}}}(a_t|s_t)} \hat{A}_t, \text{clip} \left( \frac{\pi_\theta(a_t|s_t)}{\pi_{\theta_{\text{old}}}(a_t|s_t)}, 1 - \epsilon, 1 + \epsilon \right) \hat{A}_t \right) \right], \quad (2.9)$$

where  $L^{\text{CLIP}}(\theta)$  is used to optimize the performance of the current policy, where  $\hat{\mathbb{E}}_t$  denotes the empirical expectation at time step  $t$ . The ratio of the probability of choosing action  $a_t$  under the current policy  $\pi_\theta(a_t|s_t)$  to the probability under the old policy  $\pi_{\theta_{\text{old}}}(a_t|s_t)$  is represented as  $\frac{\pi_\theta(a_t|s_t)}{\pi_{\theta_{\text{old}}}(a_t|s_t)}$ , which measures the extent of policy change. The advantage function estimate  $\hat{A}_t$  evaluates the relative value of taking action  $a_t$  in state  $s_t$ . To maintain stability in policy updates, a clipping mechanism is introduced:  $\text{clip} \left( \frac{\pi_\theta(a_t|s_t)}{\pi_{\theta_{\text{old}}}(a_t|s_t)}, 1 - \epsilon, 1 + \epsilon \right)$ , which restricts the policy ratio within the range  $[1 - \epsilon, 1 + \epsilon]$ , where  $\epsilon$  is a small hyperparameter controlling the range of the update. This objective function allows the PPO algorithm to ensure stable policy updates while optimizing the policy performance.

### 2.5. DRL-Enhanced Active Flow Control

We couple a computational fluid dynamics environment with a DRL framework to address AFC. The two core components of DRL, the agent and the environment, are integral to this approach. In our study, we utilize a PPO agent to train the control policy, while the CFD environment simulates flow around either a circular or square cylinder. The primary task of the PPO agent is to determine an optimal real-time control strategy for two jet actuators positioned on the cylinder’s surface, with the goal of minimizing the fluid forces acting on the structure. The agent obtains state information by observing the CFD environment, with flow probes measuring quantities such as velocity and pressure within the flow field. The agent’s actions involve adjusting the mass flow rate of the synthetic jets, enabling precise control over the flow dynamics. To present a clear understanding of the DRL-based AFC framework, we provide a detailed explanation of each key component: the agent, the environment, state observations, action selection, and the reward mechanism. By elaborating on these elements, we aim to clarify their roles within the system and illustrate how they interact. This detailed breakdown enhances our ability to analyze and understand the application of DRL in optimizing AFC performance.

- **Agent** : The neural network of the agent is parameterized by  $\theta$  (including weights and biases), and through training, this network learns the optimal policy  $\pi_\theta(a_t | s_t)$ , which represents the probability distribution of actions  $a_t$  given a state  $s_t$ . The objective is to

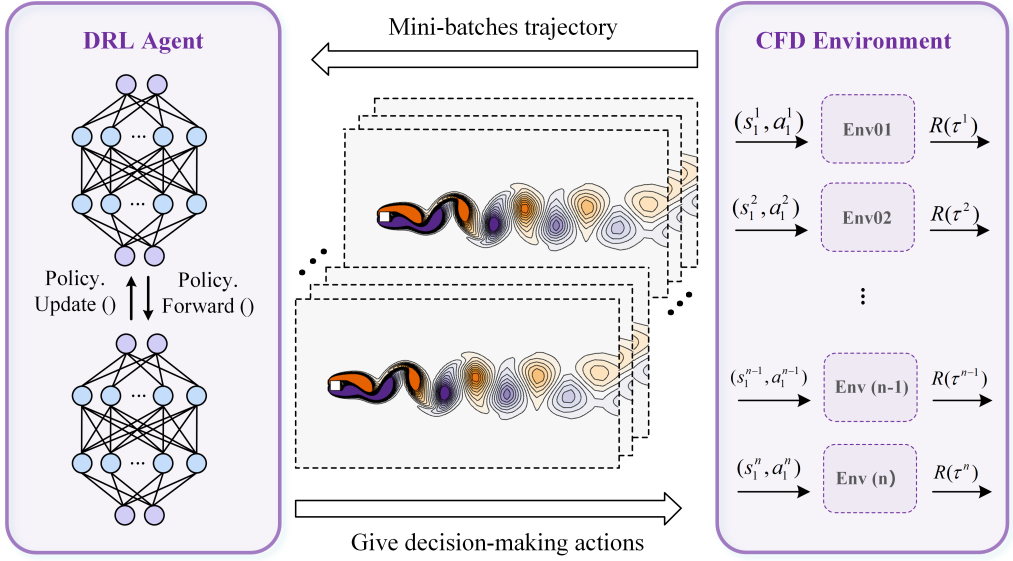


Figure 7: Schematic of the interaction between the deep reinforcement learning agent and the computational fluid dynamics environment for active flow control. The DRL agent receives state information  $s_t^i$  from the CFD environment at each timestep  $t$ , selects an action  $a_t^i$  to adjust the synthetic jets, and then the environment returns a new state  $s_{t+1}^i$  and a reward  $R(\tau^i)$ , where  $\tau^i$  represents the trajectory of states and actions. The agent updates its policy  $\pi_\theta$  to maximize the expected cumulative reward  $\mathbb{E}[R(\tau^i)]$ , optimizing flow control through iterative learning across multiple parallel environments.

maximize the expected cumulative reward  $R_t = \sum_{k>t} \gamma^{(k-t)} r_k$ , where  $\gamma \in (0, 1]$  is the discount factor. PPO is an episode-based actor-critic algorithm that includes both an actor network  $\pi_\theta$  and a critic network  $V(s_t)$ . In the PPO algorithm, the actor network is responsible for learning and outputting the policy  $\pi_\theta(a_t | s_t)$  for selecting actions in different states to maximize the cumulative reward  $R_t$ . The critic network  $V(s_t)$  evaluates the expected cumulative reward for each state  $s_t$  and provides feedback and guidance for updating the policy  $\pi_\theta$  of the actor network. Both the actor and critic networks are comprised of two fully connected layers, each with 512 units. The Adam optimizer is used for updating the networks, with a fixed learning rate of 0.001. In reinforcement learning, agent selection depends on the state space, action space, exploration-exploitation trade-off, computational resources, and objectives. For high-dimensional continuous spaces like fluid mechanics, PPO (Rabault *et al.* (2019, 2020); Tang *et al.* (2020a)), SAC (Wang *et al.* (2022a); Wang & Xu (2024d); Xia *et al.* (2024)), TD3 (Fan *et al.* (2020)) and TQC (Xia *et al.* (2024)) are ideal, with PPO excelling in real-time flow control due to its exploration balance and efficiency.

- **Environment** : the environment interacting with the agent is instantiated using CFD. We utilized the gym library interface to integrate OpenFOAM into the DRL framework. The CFD simulations are performed using the open-source software platform OpenFOAM® version 8. Figure 7 illustrates the integration of CFD computations as a DRL training environment and demonstrates the benefits of accelerating the training process by using multiple parallel CFD environments. This parallelization strategy is inspired by the work of Rabault & Kuhnle, and also incorporates insights from Wang & Xu. Research by Rabault & Kuhnle indicates that acceleration can be achieved by parallelizing both the numerical simulations and the DRL algorithm. In their study, CFD computations utilized the finite element method implemented within the FEniCS framework. Wang & Xu demonstrated that different CFD computation

platforms can significantly affect parallel acceleration. They investigated various hybrid parallelization configurations based on the OpenFOAM environment and proposed effective parallelization strategies. This study involves two flow scenarios: flow around a square cylinder and flow around a circular cylinder, which were described in detail in the previous sections. The environment depends on the type of CFD solver, and there are various codes available for coupling numerical simulation environments with RL frameworks. For example, RL has been integrated with the FEniCS environment (Rabault *et al.* (2019)), the OpenFOAM environment (Wang *et al.* (2022a)), and the Nek5000 environment (Li & Zhang (2022)).

- Action  $a_t$ : In the interaction between the agent and the environment, the actions are defined as the dimensionless mass flow rates of the synthetic jets  $Q_i$  ( $i = 1, 2$ ). To maintain a zero net mass flow rate in the system, a mass balance constraint  $Q_1 + Q_2 = 0$  is imposed. This constraint not only ensures the physical conservation of mass but also significantly enhances the stability of the numerical simulations by mitigating errors associated with imbalanced flows. Furthermore, to prevent non-physical large actuation that could destabilize the system, a limit is imposed on the normalized mass flow rate, such that  $|Q_i^*| < 0.06$ .  $Q_i^*$  denotes the normalized mass flow rate, defined as  $Q_i/Q_{\text{ref}}$ , where  $Q_{\text{ref}} = \int_{-D/2}^{D/2} \rho U(y) dy$  serves as the reference mass flow rate, based on the fluid density and velocity distribution. This constraint effectively regulates the jet intensity, thereby ensuring both stability and accuracy in the flow control process, leading to more precise and reliable numerical results. To further ensure stability and mitigate non-physical instabilities in the flow, a smoothing function is applied, where  $V_{\Gamma_1, T_i}$  represents the jet velocity at the end of the  $i$ th actuation control period  $T_i$ , and  $\beta$  is a numerical smoothing parameter:

$$V_{\Gamma_1, T_i} = V_{\Gamma_1, T_i} + \beta (a - V_{\Gamma_1, T_{i-1}}). \quad (2.10)$$

- State  $s_t$ : The agent observes the state of the CFD environment by collecting physical field data from specific locations within the computational domain. Building on previous studies, such as those by Wang *et al.*, who utilize velocity probes, and Rabault *et al.*, who employ pressure probes to capture instantaneous pressure at key points, we draw inspiration from Li & Zhang to strategically place observation probes at locations within the flow field where fluctuations are most pronounced. These probes are situated in regions of the wake characterized by the weakest stability and highest sensitivity, allowing for more effective flow control through the monitoring of time-averaged fluctuating pressure. This targeted placement optimizes the control strategy by focusing on the most critical areas of the flow, thereby enhancing both the efficiency and effectiveness of the flow control efforts. In addition to positioning probes within the wake region, we also place probes around the circumference of the cylinder to extract physical information from its surface, which is closely related to the lift and drag on the cylinder. For more details on the number and distribution of these probes, readers can refer to the studies by Paris *et al.*; Li & Zhang; Wang *et al.*, who have conducted in-depth discussions on this topic.

- Reward  $r_t$ : The design of the reward function is based on the overall objective of flow control, making the selection of appropriate performance metrics crucial for the convergence and stability of reinforcement learning. In this study, we aim for flow control to reduce both drag and lift around the cylinder. Therefore, we construct the reward function based on the drag coefficient ( $C_D$ ) and the lift coefficient ( $C_L$ ). The specific reward function is defined as follows:

$$r_{T_i} = C_{D,0} - (C_D)_{T_i} - \omega |(C_L)_{T_i}|, \quad (2.11)$$

where,  $C_{D,0}$  represents the baseline drag coefficient, serving as a reference to encourage positive rewards and facilitate convergence during training. The term  $(C_D)_{T_i}$  denotes the drag coefficient at time step  $T_i$ , with the objective of minimizing it relative to the baseline.

The lift coefficient  $(C_L)_{T_i}$  is also included, with its absolute value penalized to mitigate instabilities caused by lift around the bluff body. The parameter  $\omega$  is a weighting factor used to balance the trade-off between reducing drag and controlling lift. Given the directional nature of the flow under consideration,  $\omega$  is typically set between 0.1, 0.2 and 1, reflecting the relative importance of minimizing drag over controlling lift fluctuations. In previous work, the lift coefficient penalty factor is often set to 0.1 (Wang & Xu 2024c), 0.2 (Rabault *et al.* 2019; Tang *et al.* 2020b), or 1 (Ren *et al.* 2021). In this study, we use a penalty factor of 0.2, consistent with Rabault *et al.*.

- **Interaction:** In DRL, the interaction between the agent and the environment forms the foundation of the learning process. At each time step  $t$ , the agent first gathers physical data regarding the current flow state  $s_t$  from the CFD environment. Based on this information, the agent selects an action  $a_t$  according to its control policy  $\pi_\theta(a_t | s_t)$ . This selected action  $a_t$  is then communicated to the CFD environment, which executes the action, transitions to the next state  $s_{t+1}$ , and provides an immediate reward  $r_t$ . The agent, in turn, receives both the reward  $r_t$  and the updated physical state information  $s_{t+1}$ , using this feedback to refine its control policy  $\pi_\theta$  in order to maximize cumulative future rewards  $\sum_t \gamma^t r_t$ , where  $\gamma$  is the discount factor. This iterative cycle continues until the task is accomplished or a predefined termination condition is met.

Through successive interactions, the agent incrementally optimizes its control policy  $\pi_\theta$  via trial and error, ultimately mastering the dynamic adjustment of jet velocity  $V_\Gamma$  in real-time to achieve optimal flow control performance. In this study, the total number of DRL training episodes is set to 3,000, with each episode consisting of 100 training timesteps. Each timestep corresponds to a non-dimensional time of 0.025, resulting in a maximum duration per episode of  $T_{\max} = 2.5$ . This duration spans approximately 8 to 10 vortex shedding cycles, during which 100 control actions are executed. Training the DRL agent over multiple vortex shedding cycles ensures that the agent fully captures the complex flow dynamics, stabilizes the learning process, and develops a robust and generalizable control strategy for effective flow management.

### 3. Results: flow control performance of a circular cylinder

In this section, we employ the flow around a cylinder as the DRL training environment, utilizing the control capabilities of a PPO agent to achieve active flow control through synthetic jets, with the primary objectives of drag reduction and vortex suppression. The focus of this study is to investigate how the positioning of synthetic jets affects flow control performance and the associated costs, with the aim of deriving qualitative insights through rigorous physical analysis. The cost of implementing flow control is quantified by the dimensionless mass flow rates of the synthetic jets. To explore the effects of jet positioning, we design five configurations involving a single pair of synthetic jets, two configurations involving two pairs of synthetic jets, and one additional configuration with a single pair of synthetic jets. Each scheme is carefully constructed to assess the influence of jet distribution on the overall flow control effectiveness and efficiency.

#### 3.1. A pair of synthetic jets controllers

##### 3.1.1. Scenario A: Control Performance of Jet Pair

We compare the performance and effectiveness of flow control strategies obtained through DRL training with synthetic jets placed at different positions on the cylinder surface. These five synthetic jets configurations are designed based on the angular positions on the cylinder, ranging from  $60^\circ$  to  $120^\circ$ . In these configurations, the  $J_1$  setup includes two jets,  $J_1^1$  and  $J_1^2$ ,



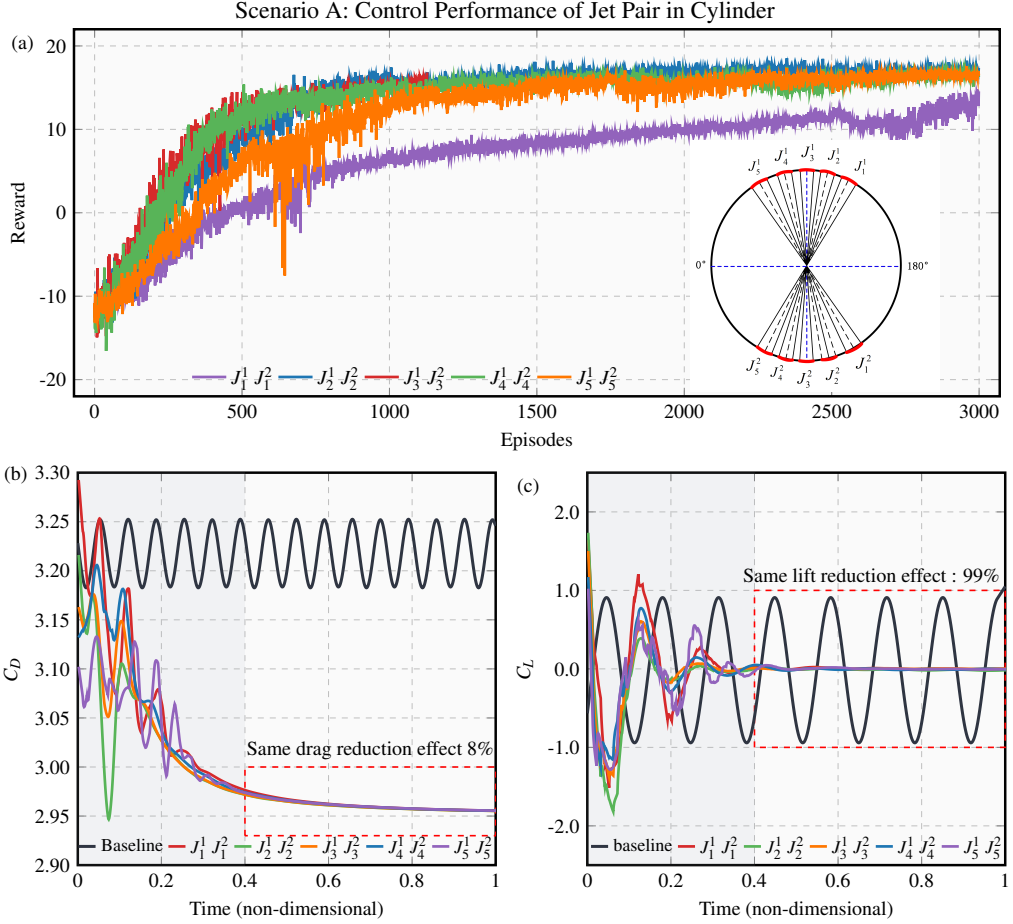


Figure 8: Performance evaluation of different jets configurations for flow control around a cylinder. (a) Reward curves over training episodes for various jets positions. (b) Drag coefficient  $C_D$  over non-dimensional time, comparing the baseline scenario with different jets configurations. (c) Lift coefficient  $C_L$  over non-dimensional time, comparing the baseline scenario with different jets configurations.

with  $J_1^1$  located at an angular position of  $120^\circ$ . The  $J_3$  setup includes two jets,  $J_3^1$  and  $J_3^2$ , with  $J_3^1$  located at  $90^\circ$ . The  $J_5$  setup also includes two jets,  $J_5^1$  and  $J_5^2$ , with  $J_5^1$  located at  $60^\circ$ .

As shown in figure 8, the reward function curves reflect how the performance of the DRL agent evolves as training progresses. In the early stages of training, the reward function curves often exhibit significant fluctuations, indicating the exploration and experimentation phase of the agent within the strategy space. As training continues, the agent gradually optimizes its strategy, leading to an upward trend in the reward function values, which suggests that the agent is effectively learning the flow control strategy. By comparing the learning curves for different jet positions, we observe that when the jets are positioned at  $J_1$ , the reward function grows most slowly and reaches the lowest final value, indicating that the flow control strategy at this position is more challenging to converge. In contrast, when the jets are positioned at  $J_5$ , the learning curve shows a slightly faster growth but still lags behind others, indicating a moderate difficulty in strategy convergence. Conversely, when the jets are positioned at  $J_2$ ,

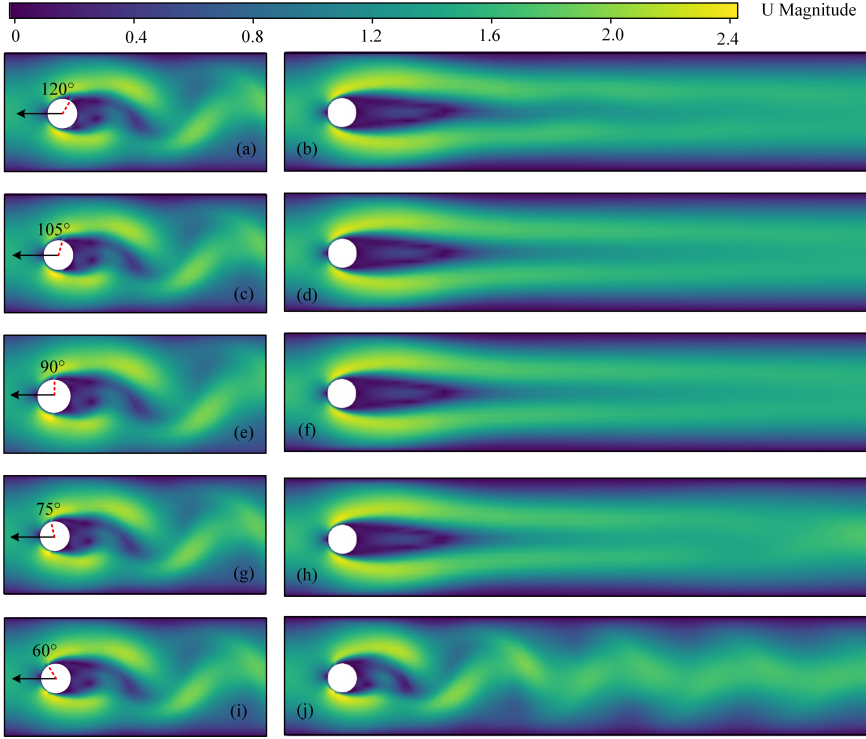


Figure 9: Velocity contours of flow around a cylinder with synthetic jets at various angular positions. The left column shows the jet activation, and the right column shows the corresponding control results. (a) and (b) Jets at  $120^\circ$ , (c) and (d) at  $105^\circ$ , (e) and (f) at  $90^\circ$ , (g) and (h) at  $75^\circ$ , and (i) and (j) at  $60^\circ$ .

$J_3$ , and  $J_4$ , the DRL agent achieves rapid convergence within 1,000 episodes, demonstrating that the flow control strategies at these positions are easier to learn and optimize. Between 1,000 and 3,000 episodes, the reward function curves plateau, indicating that the DRL agent has successfully mastered a stable and effective flow control strategy. At this stage, the reward values remain stable, further confirming the effectiveness and reliability of the learned strategy in reducing drag and controlling lift.

The baseline  $C_D$  represents the scenario without any active flow control and serves as a reference point. As shown in figure 8, all jet configurations achieve a reduction in  $C_D$ , with drag reduction of approximately 8% across the five jet positions. This indicates that the DRL-optimized jet actuation effectively reduces the drag experienced by the cylinder, with the curves stabilizing after the initial transient phase, suggesting that the control actions lead to a steady reduction in drag. For the same jet configurations, the baseline  $C_L$  exhibits significant fluctuations, which are common in flows past bluff bodies such as cylinders. The DRL-controlled jets achieve a substantial reduction in these fluctuations, with the lift oscillations being nearly eliminated in all five jet positions, resulting in up to a 99% reduction in  $C_L$  oscillations. The dramatic reduction in lift fluctuations indicates that the jets not only reduce drag but also stabilize the flow, preventing lift-induced instabilities that could otherwise affect the effectiveness of flow control. The stabilization of the drag and lift coefficients over time demonstrates that the learned strategies are both effective and stable. The DRL training curves illustrate the learning process of the agent, resulting in an optimized control strategy that effectively reduces both drag and lift coefficients. The significant drag reduction and

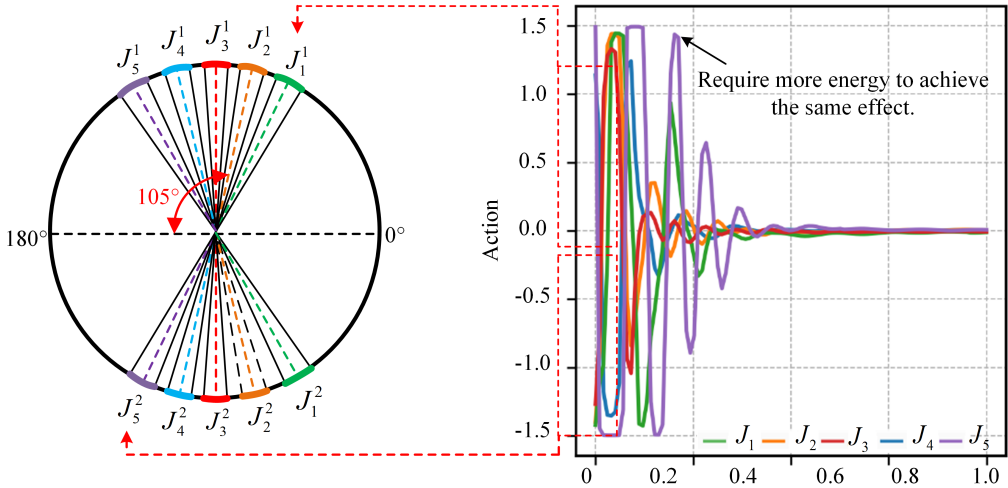


Figure 10: Energy consumption analysis of jet pairs positioned at different angular locations around a cylinder. The left panel illustrates the angular placement of jet pairs  $J_1$  through  $J_5$  around the cylinder, while the right panel shows the corresponding action values over non-dimensional time for each jet configuration.

near-complete suppression of lift fluctuations highlight the potential of DRL in achieving robust and efficient flow control in real-time applications.

The activation states of synthetic jets at various azimuthal angles, along with the corresponding controlled flow fields, are illustrated in figure 9. When the activation states of synthetic jets at different azimuthal angles are shown in the left column of figure 9, the pair of synthetic jets symmetric about the x-axis alternately engage in blowing or suction phases. With the jets positioned at  $J_1$  at  $120^\circ$ , the velocity contours show the development of a large recirculation region on the cylinder's rear side, despite minor oscillations in the wake. When the jets are positioned at  $J_2$  at  $105^\circ$  and  $J_3$  at  $90^\circ$ , vortex shedding in the wake is fully suppressed, indicating that jets at these locations can effectively delay separation, reduce the separation zone, and even eliminate it, thereby reducing drag. For  $J_4$  at  $75^\circ$ , the wake is largely stabilized, though weak oscillations persist downstream. Glezer & Amitay (2002) used smoke flow visualization to show that a synthetic jet at an injection angle of  $\gamma = 60^\circ$  caused local deformation of the streaklines on the upper surface of the cylinder, shifting the separation point downstream and the front stagnation point below the x-axis. When the jet is set at  $\gamma = 60^\circ$ , our reinforcement learning algorithm achieves similar control performance over the cylinder flow field as observed by Glezer & Amitay (2002), with periodic vortex shedding still evident in the controlled flow. The effectiveness of flow control varies significantly with jet positioning, with the least effective control observed at  $J_1$  ( $120^\circ$ ) and  $J_5$  ( $60^\circ$ ), where the jets can still delay separation.

### 3.1.2. Scenario A: Energy Consumption of Jet Pair

A detailed analysis of the energy consumption associated with various jet configurations around a cylinder, along with their effectiveness in flow control, is presented in figure 10. The figure depicts the angular placement of five jet pairs ( $J_1$  through  $J_5$ ) along the cylinder surface, with  $J_1$  located nearest to the forward stagnation point ( $0^\circ$ ) and  $J_5$  positioned further downstream. These jet pairs are symmetrically distributed on both sides of the cylinder's centerline, covering angular positions from  $120^\circ$  to  $60^\circ$ . The right side of the figure shows the action values, representing the intensity of jet actuation, plotted over non-dimensional time

for each jet configuration, thereby providing insight into the energy consumption required to achieve the desired flow control.

The curves for each configuration initially exhibit a peak, representing the maximum energy required at the onset of jet actuation. Notably, the curves for  $J_5$  and  $J_1$  display the highest initial action values, indicating that these positions demand more energy to initiate flow control compared to other configurations. Following the initial transient phase, the action values stabilize, signifying that the control effort, and thus energy consumption, becomes more consistent over time. The action values for configurations  $J_2$ ,  $J_3$ , and  $J_4$  stabilize at lower levels than those for  $J_5$  and  $J_1$ , suggesting that these configurations are more energy-efficient in maintaining flow control. The annotations on the plot highlight that energy consumption peaks around the  $90^\circ$  position, while it remains comparable at  $75^\circ$  and  $105^\circ$ . This observation implies that jets positioned at  $60^\circ$  and  $120^\circ$  (such as  $J_5$  and  $J_1$ ) are less energy-efficient, requiring more energy to achieve the same flow control effect as the more efficiently positioned jets at  $90^\circ$  and  $105^\circ$ . This insight highlights the critical importance of optimizing jet positioning to minimize energy consumption, a key consideration in designing efficient flow control systems that maximize aerodynamic performance while reducing power requirements around the cylinder.

### 3.2. Multiple pairs of synthetic jets controllers

#### 3.2.1. Scenario B: Control Performance of Multiple Jets Control

Based on the results of flow control using a single pair of synthetic jets, it was observed that the configurations with jets positioned at  $60^\circ$  and  $120^\circ$  ( $J_5$  and  $J_1$ ) consumed the most energy. Consequently, when employing multiple pairs of synthetic jets for flow control, we excluded the jets positioned at  $60^\circ$  and  $120^\circ$ , focusing instead on combinations involving  $J_2$ ,  $J_3$ , and  $J_4$ . The configurations tested include two pairs of synthetic jets ( $J_2$  and  $J_3$ ;  $J_3$  and  $J_4$ ) and a configuration with three pairs ( $J_2$ ,  $J_3$ , and  $J_4$ ). To investigate the control performance and convergence speed of multiple synthetic jets combinations compared to single-pair synthetic jets, we analyze the control performance of single-pair synthetic jets ( $J_2$ ,  $J_3$ , and  $J_4$ ) as the control group.

The performance of multiple jet configurations used for flow control around a cylinder, evaluated through deep Reinforcement Learning training, is comprehensively analyzed in figure 11(a). The reward curves reflect the effectiveness of the DRL agent in learning flow control strategies using different combinations of synthetic jets configurations. Across various configurations, the reward function exhibits a stepwise increase during the initial training phase. As training progresses, the reward values reach a plateau, indicating that the agent has successfully optimized its control strategy. However, different configurations display varying convergence speeds. It is observed that employing multiple pairs of synthetic jets for flow control does not accelerate the reinforcement learning training process. The reward function for single-pair synthetic jets converges more rapidly than that for multiple pairs, suggesting that single-pair jet configurations are more conducive to faster convergence and more effective for the agent to learn the control strategy.

The variation of the drag coefficient with non-dimensional time for different jet configurations is illustrated in figure 11(b). The curves indicate that all jet configurations achieve similar drag reduction, with the drag coefficient stabilizing after the initial transient phase. This stabilization suggests that the control strategies are effective in maintaining a consistent reduction in drag over time. The variation of the lift coefficient with non-dimensional time, demonstrating the effectiveness of the jet configurations in reducing lift fluctuations, is shown in figure 11(c). The results reveal a significant reduction in lift oscillations across all jet configurations, with the lift coefficient stabilizing near zero after the initial transient phase.

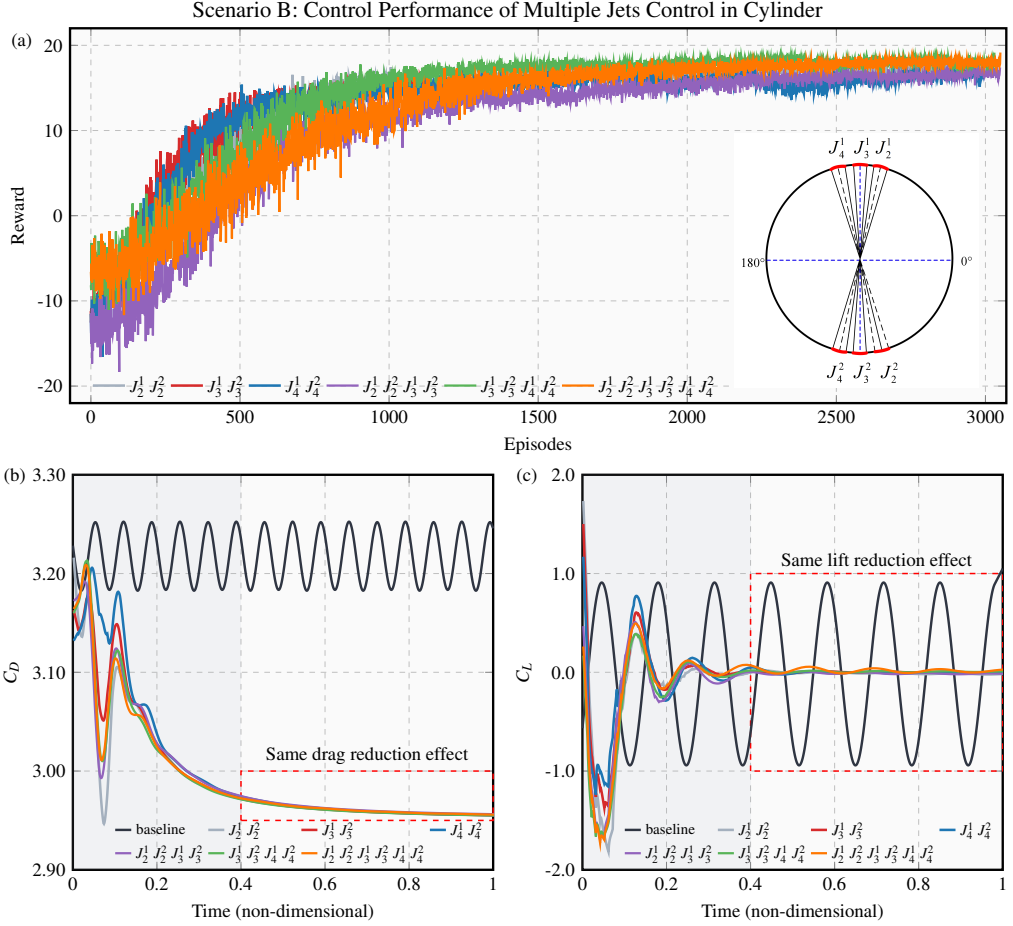


Figure 11: Control performance evaluation of multiple jet configurations around a cylinder. (a) Reward curves over training episodes for various multi-jet configurations. (b) Drag coefficient  $C_D$  over non-dimensional time. (c) Lift coefficient  $C_L$  over non-dimensional time.

Similar to the drag coefficient, the consistent performance across configurations reinforces the conclusion that these jet positions are effective and efficient for flow control. Additionally, we observe that the synthetic jets positioned at  $105^\circ$  ( $J_1^1$  and  $J_2^1$ ) exhibit a more pronounced transient response in both drag and lift coefficients, indicating a higher sensitivity to the jet actuation. This is a subtle but important observation that will be discussed further in subsequent sections.

### 3.2.2. Scenario B: Energy Consumption with Simultaneous Control (Two Pairs)

We execute flow control with a strategy involving the mass flow rates of two pairs of synthetic jets, referred to as Action in figure 12. The action values, representing the external energy consumed, are plotted over non-dimensional time for various jet configurations around the cylinder. Figure 12(a) depicts the control strategy utilizing two pairs of synthetic jets ( $J_3^1, J_3^2$  and  $J_4^1, J_4^2$ ). The initial peak in action values indicates the maximum energy required at the onset of the flow control process. As time progresses, the energy consumption stabilizes,

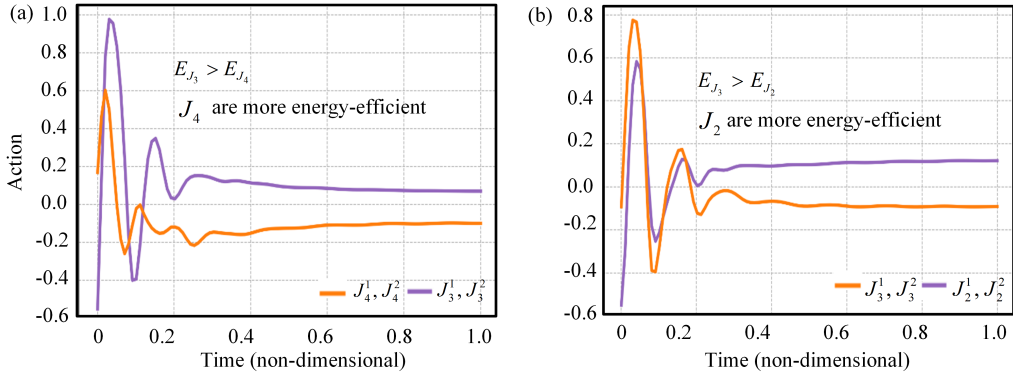


Figure 12: Comparison of action values over non-dimensional time for different synthetic jets configurations around the cylinder. (a) Two pairs of jets:  $J_3^1, J_3^2$  and  $J_4^1, J_4^2$ . (b) Two pairs of jets:  $J_2^1, J_2^2$  and  $J_3^1, J_3^2$ .

suggesting that the control strategy becomes more consistent. We observe that the jet pair  $J_4^1, J_4^2$  consumes slightly less energy in the long run compared to  $J_3^1, J_3^2$ , indicating that positioning synthetic jets at  $J_4$  ( $75^\circ$ ) may offer an energy-saving advantage over positioning at  $J_3$  ( $90^\circ$ ).

The energy consumption for the control strategy utilizing two pairs of synthetic jets ( $J_3^1, J_3^2$  and  $J_2^1, J_2^2$ ) is shown in figure 12(b). The initial action peak is again prominent, reflecting the energy required at the start of the flow control process. Over time, both configurations exhibit reduced energy consumption, with action values stabilizing. However, jet pair  $J_3^1, J_3^2$  demonstrates a slightly higher energy demand over time compared to  $J_2^1, J_2^2$ , suggesting that  $J_2^1, J_2^2$  may be more energy-efficient in maintaining effective flow control. This analysis provides a deeper understanding of the energy efficiency of different jet configurations in controlling flow around the cylinder. The initial peaks highlight the energy demands at the start, while the subsequent stabilization reflects the sustained maintenance of flow control. The differences in energy consumption among configurations can guide the selection of jet positions to optimize flow control efficiency, with the  $J_4$  position ( $75^\circ$ ) and  $J_2$  position ( $105^\circ$ ) showing potential as a more energy-efficient choice.

### 3.2.3. Scenario B: Energy Consumption with Simultaneous Control (Three Pairs)

A detailed analysis of energy consumption during flow control using three pairs of synthetic jets is presented in figure 13. These jets ( $J_2^1, J_2^2, J_3^1, J_3^2$ , and  $J_4^1, J_4^2$ ) are symmetrically arranged around the cylinder at angular positions of  $75^\circ$  ( $J_4$ ),  $90^\circ$  ( $J_3$ ), and  $105^\circ$  ( $J_2$ ) relative to the forward stagnation point ( $0^\circ$ ). The action values shown in figure 13 correspond to the external energy expenditure associated with jet operation over non-dimensional time. In this context,  $E_{J_3}$  denotes the external energy required by the synthetic jets pair  $J_3$ , comprising  $J_3^1$  and  $J_3^2$ , to achieve effective flow control. Interestingly, when compared to figure 12, where only two pairs of synthetic jets are employed, figure 13 demonstrates that the activation of three pairs of synthetic jets leads to a reduction in the peak external energy demand for each individual jet. This suggests that the simultaneous use of additional jets can distribute the energy load more effectively, thereby enhancing the overall efficiency of the flow control strategy.

At the onset, the action values across all three configurations, as optimized via DRL, exhibit pronounced peaks. Following the initial transient phase, the energy consumption stabilizes across all configurations, indicating a uniform energy requirement as the flow

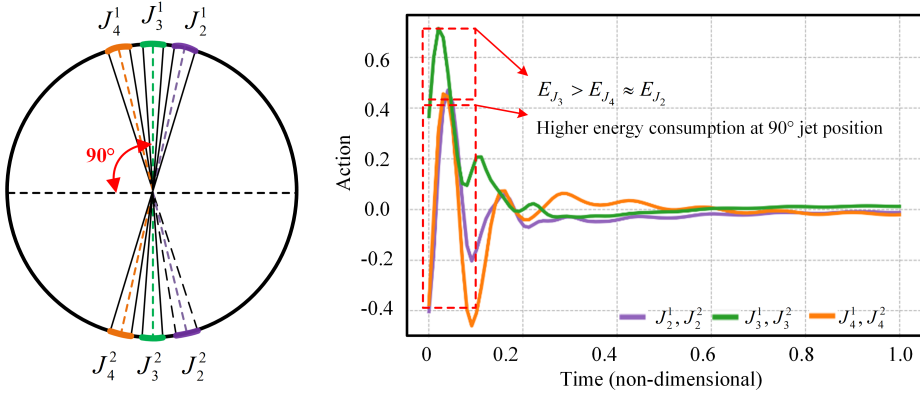


Figure 13: Energy consumption analysis for different jet pairs positioned around a cylinder. The left diagram illustrates the angular positions of the jet pairs  $J_2^1, J_3^1, J_4^1$  on the upper half and  $J_2^2, J_3^2, J_4^2$  on the lower half, with angles ranging from  $75^\circ$  to  $105^\circ$ . The right graph displays the corresponding action values over non-dimensional time for each jet configuration.

control reaches a steady state. The jet pair positioned at  $90^\circ$  ( $J_3$ ) demonstrates the highest peak, suggesting that the energy consumption at the  $90^\circ$  jet position ( $E_{J_3}$ ) is significantly higher than that of the other two configurations ( $E_{J_4} \approx E_{J_2}$ ). This observation implies that the  $90^\circ$  jet position demands greater energy to achieve comparable control efficacy, thereby indicating a lower energy efficiency compared to the  $75^\circ$  and  $105^\circ$  positions. The variations in energy consumption associated with different jet positions for flow control around a cylinder, emphasizing the critical importance of selecting an optimal jet position to minimize energy consumption while maintaining effective flow regulation, are highlighted in figure 13. The results suggest that the jet positions at  $75^\circ$  ( $J_4$ ) and  $105^\circ$  ( $J_2$ ) exhibit similar and reduced energy demands, indicating their superiority in sustaining flow control. Conversely, although the  $90^\circ$  position is frequently utilized in flow control applications, it may not represent the most energy-efficient choice. These findings are vital for refining flow control strategies, particularly in scenarios where energy efficiency is of paramount importance.

#### 4. Results: flow control performance of a square cylinder

In this section, we use the flow around a square cylinder as the DRL training environment, employing the control capabilities of a PPO agent to implement active flow control through synthetic jets positioned near the front and rear corners of the cylinder. The flow around a square cylinder is characterized by earlier separation at sharp edges, more complex and turbulent wake structures, and greater flow instability compared to a circular cylinder, making it more challenging to control. This study aims to understand how the positioning of synthetic jets influences flow control performance and costs in this context. To explore these effects, we design four configurations with a single pair of synthetic jets, one configuration with two pairs of synthetic jets, and one additional configuration with a single pair of synthetic jets. These configurations are specifically designed to assess the impact of jet placement on the effectiveness and efficiency of flow control.

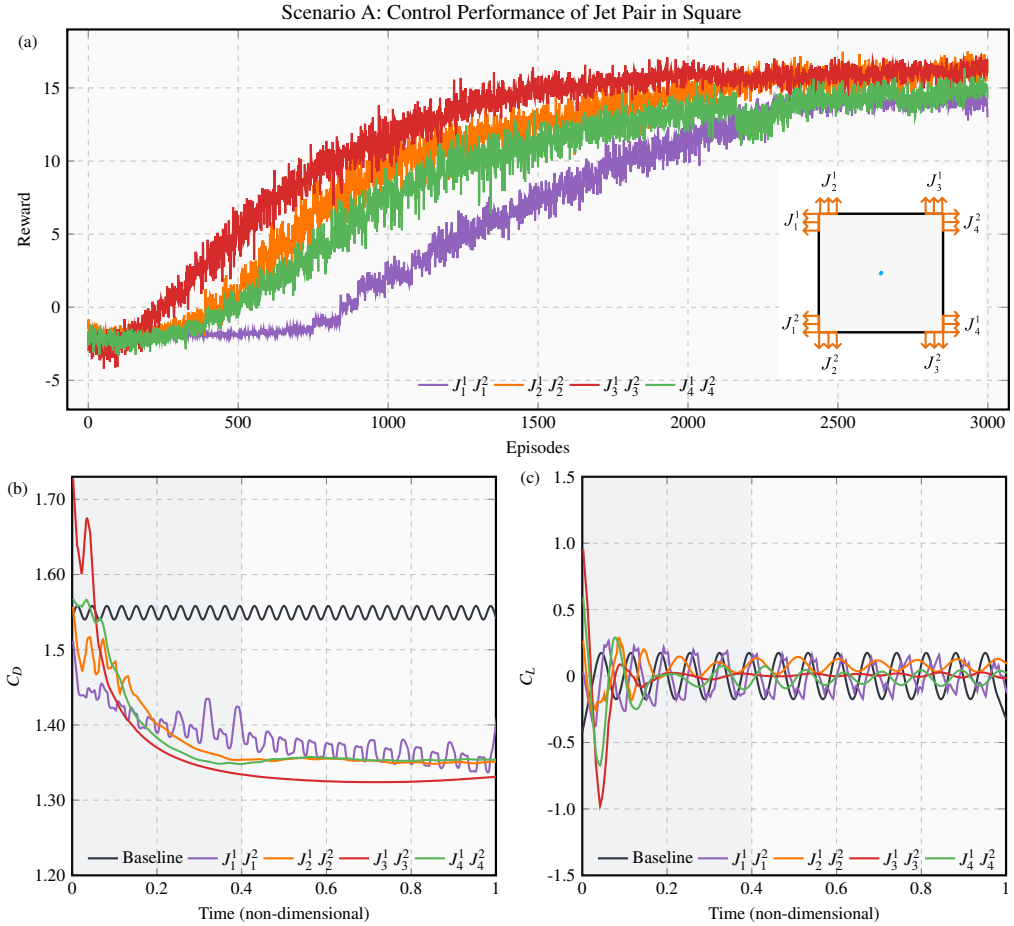


Figure 14: Performance evaluation of different jet configurations for flow control around a square cylinder. (a) Reward curves over training episodes for various jet positions. (b) Drag coefficient  $C_D$  over non-dimensional time, comparing the baseline scenario with different jets configurations. (c) Lift coefficient  $C_L$  over non-dimensional time, comparing the baseline scenario with different jets configurations.

#### 4.1. A pair of synthetic jets controllers

##### 4.1.1. Scenario A: Control Performance of Jet Pair

In this study, we use DRL to develop flow control strategies for the flow around a square cylinder, as shown in figure 14. The figure provides a detailed analysis of the influence of synthetic jet positioning on flow control performance within the square geometry. The reward function serves as the primary metric for evaluating the effectiveness of the control strategies developed by the DRL agent. Initially, the reward values are low, reflecting the early stages of learning and the exploration of suboptimal strategies. As training progresses, a significant increase in the reward function is observed across all jet configurations, particularly between the 500th and 2000th episodes. This trend indicates that the DRL agent is successfully optimizing the control strategies, leading to improved flow control. The consistent rise in the reward function suggests that the DRL algorithm is steadily refining its policy, converging



toward an optimal solution. The agent's ability to adapt and improve through continuous learning highlights the potential of DRL in addressing complex flow control challenges.

We examined the reward function behavior during DRL training with synthetic jets positioned near the front and rear corners of a square cylinder, specifically for the configurations  $J_2^1, J_2^2, J_3^1, J_3^2$ , and  $J_4^1, J_4^2$ , as illustrated in figure 14(a). Our findings reveal that the reward function experienced the most rapid growth when the jets were located at  $J_3^1, J_3^2$ , whereas the slowest growth occurred for the  $J_2^1, J_2^2$  configuration. This variation in growth rates underscores the superior adaptability of the  $J_3^1, J_3^2$  configuration, as it allows the DRL agent to more effectively achieve the control objectives. The accelerated increase in the reward function associated with  $J_3^1, J_3^2$  indicates that this setup is intrinsically more aligned with the flow control requirements, facilitating a more efficient optimization process.

In contrast, the slower growth observed for  $J_2^1, J_2^2$  suggests that this configuration may encounter challenges in interacting with the flow dynamics, potentially due to a more complex flow behavior that hinders the learning efficiency of the agent. These findings highlight the critical role of jet positioning in optimizing flow control strategies. The distinct differences in reward growth rates not only reflect the varying degrees of learning efficiency but also emphasize the importance of strategic jet placement in enhancing the performance of DRL-based flow control. Configurations like  $J_3^1, J_3^2$ , which demonstrate rapid reward growth, are evidently more conducive to achieving efficient and precise flow manipulation, whereas slower growth configurations, such as  $J_2^1, J_2^2$ , may require more refined strategies or adjustments to overcome inherent complexities. These insights are vital for refining jet configurations and advancing the effectiveness of DRL algorithms in complex fluid dynamics applications.

We present the relationship between the drag coefficient and non-dimensional time for four different jet placement configurations, compared to the baseline case without active control, as shown in figure 14(b). The baseline curve, representing the drag coefficient without control, exhibits periodic oscillations. Once the synthetic jets are activated, the drag coefficient of the square cylinder decreases significantly across all configurations. The most notable reduction occurs when the jets are positioned near the rear corner points at  $J_3^1, J_3^2$ , indicating this placement is the most effective for drag reduction. In contrast, jets placed near the front corners at  $J_1^1, J_1^2$  show a clear reduction in drag, but with transient spikes and oscillations, suggesting a dynamic interaction between the jets and the flow. Configurations at  $J_2^1, J_2^2$  and  $J_4^1, J_4^2$  also result in substantial drag reduction, though less pronounced than at  $J_3^1, J_3^2$ . This analysis highlights the critical role of jet placement in optimizing flow control and reducing aerodynamic drag around square cylinders.

We depict the relationship between the lift coefficient and non-dimensional time for various synthetic jets configurations, compared to the baseline scenario, as shown in figure 14(c). The baseline lift coefficient exhibits periodic fluctuations throughout the time series, characteristic of the natural vortex shedding around the square cylinder. When the synthetic jets are positioned at  $J_2^1, J_2^2, J_3^1, J_3^2$ , and  $J_4^1, J_4^2$ , a significant attenuation in the lift coefficient is observed. Specifically, the configuration at  $J_3^1, J_3^2$  induces the most pronounced initial reduction in the lift coefficient, which rapidly stabilizes near zero, indicating effective suppression of the unsteady aerodynamic forces. Furthermore, the configurations at  $J_2^1, J_2^2$  and  $J_4^1, J_4^2$  lead to a marked reduction in both the amplitude and frequency of the lift coefficient oscillations, thereby significantly damping the lift fluctuations. This suggests a successful mitigation of vortex-induced forces through controlled jet actuation. However, when the jets are located at  $J_1^1, J_1^2$ , the lift coefficient fails to exhibit a similar reduction. Instead, transient spikes and persistent oscillations are present, indicating that this jet configuration is less effective in altering the flow structures responsible for lift generation. These results

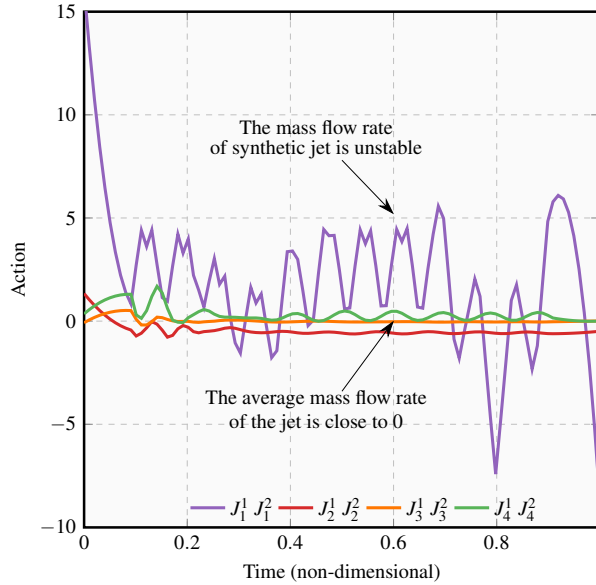


Figure 15: Energy consumption over non-dimensional time for jet pairs positioned at various locations around the square cylinder. The jet pair locations include:  $J_1^1, J_1^2$ ,  $J_2^1, J_2^2$ ,  $J_3^1, J_3^2$ , and  $J_4^1, J_4^2$ .

crystallize the crucial role of optimal jet placement in flow control, where precise modulation of aerodynamic forces, such as lift, is essential for achieving effective performance. Jet configurations that interact favorably with the complex flow dynamics around the square cylinder are the most effective in stabilizing the flow and reducing oscillatory forces.

#### 4.1.2. Scenario A: Energy Consumption of Jet Pair

The external energy consumed for flow control varies significantly with the positioning of the synthetic jets at  $J_1^1, J_1^2, J_2^1, J_2^2, J_3^1, J_3^2$ , and  $J_4^1, J_4^2$ . The time evolution of energy consumption for these different configurations is illustrated in figure 15. When the jets are located at  $J_1^1, J_1^2$ , the energy required for flow control is substantially higher, accompanied by pronounced fluctuations, indicating instability in mass flow rates. This instability suggests lower control efficiency due to complex interactions with the flow field, making it difficult to achieve consistent and effective flow manipulation. In contrast, when the jets are positioned at  $J_2^1, J_2^2, J_3^1, J_3^2$ , and  $J_4^1, J_4^2$ , the control strategies exhibit more stable behavior, with minimal oscillations and near-zero values, reflecting efficient and balanced flow control with lower energy input. Notably, the  $J_3^1, J_3^2$  configuration requires the least energy at the onset of control and remains the most stable over time. The comparison between the less stable  $J_1^1, J_1^2$  configuration and the more stable configurations highlights the differences in energy efficiency and control stability. The larger and more unstable fluctuations observed with  $J_1^1, J_1^2$  indicate lower energy efficiency and greater challenges in maintaining flow control. In contrast,  $J_3^1, J_3^2$  demonstrates more predictable and controlled energy usage, effectively sustaining flow control with lower energy costs.

In figure 16, the activation states of the synthetic jets at positions  $J_1, J_2, J_3$ , and  $J_4$  are depicted, along with the velocity contours of the flow field after flow control is completed. The velocity contours show that when the jets are positioned near the rear sides of the square cylinder at  $J_3$ , vortex shedding in the wake is fully suppressed. At  $J_4$ , located on the rear face

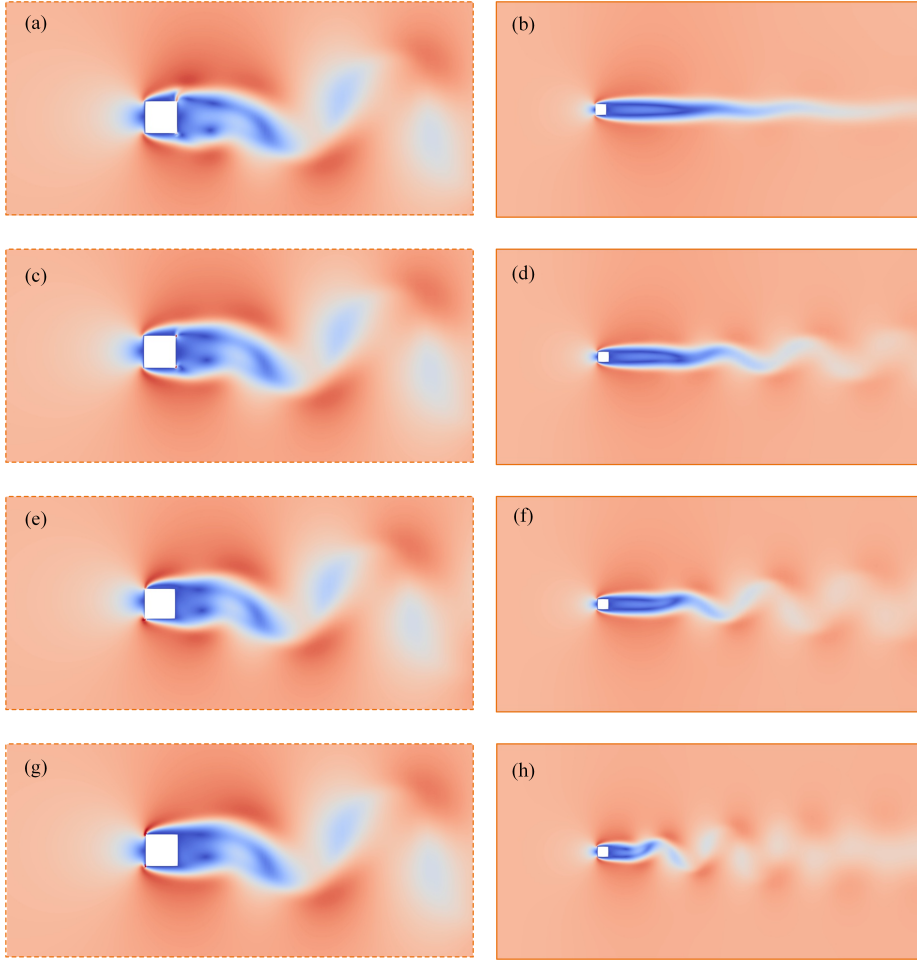


Figure 16: Velocity contours of flow around a square cylinder with synthetic jets positioned at various locations. The left column shows the flow with active jet control, while the right column presents the corresponding flow control results. (a) and (b) Jets  $J_3^1$  and  $J_3^2$  on the top and bottom sides near the rear corners. (c) and (d) Jets  $J_4^1$  and  $J_4^2$  on the rear side. (e) and (f) Jets  $J_2^1$  and  $J_2^2$  on the top and bottom sides near the front corners. (g) and (h) Jets  $J_1^1$  and  $J_1^2$  on the front side.

of the cylinder, the recirculation region expands significantly compared to the initial stages of control. When the jets are placed closer to the upstream at  $J_2$ , periodic actuation of the synthetic jets enhances the flow stability around the cylinder. Finally, at  $J_1$ , positioned at the front of the cylinder, the interaction between the synthetic jets and the free stream improves flow stability, although alternating vortex shedding still persists.

Overall, the control performance of the jets varies significantly with placement. When the synthetic jets are positioned near the front corner points, vortex shedding is not fully suppressed due to the large separated flow reattaching along the sides of the square cylinder before separating again near the rear corners. In contrast, placing the jets near the rear corner points at position  $J_3$  provides more effective flow control, leading to the complete suppression of vortex shedding. [Chen \*et al.\* \(2023\)](#) used DRL-based flow control to reduce vortex-induced vibrations around a square cylinder ( $Re = 100$ ) and compared the control

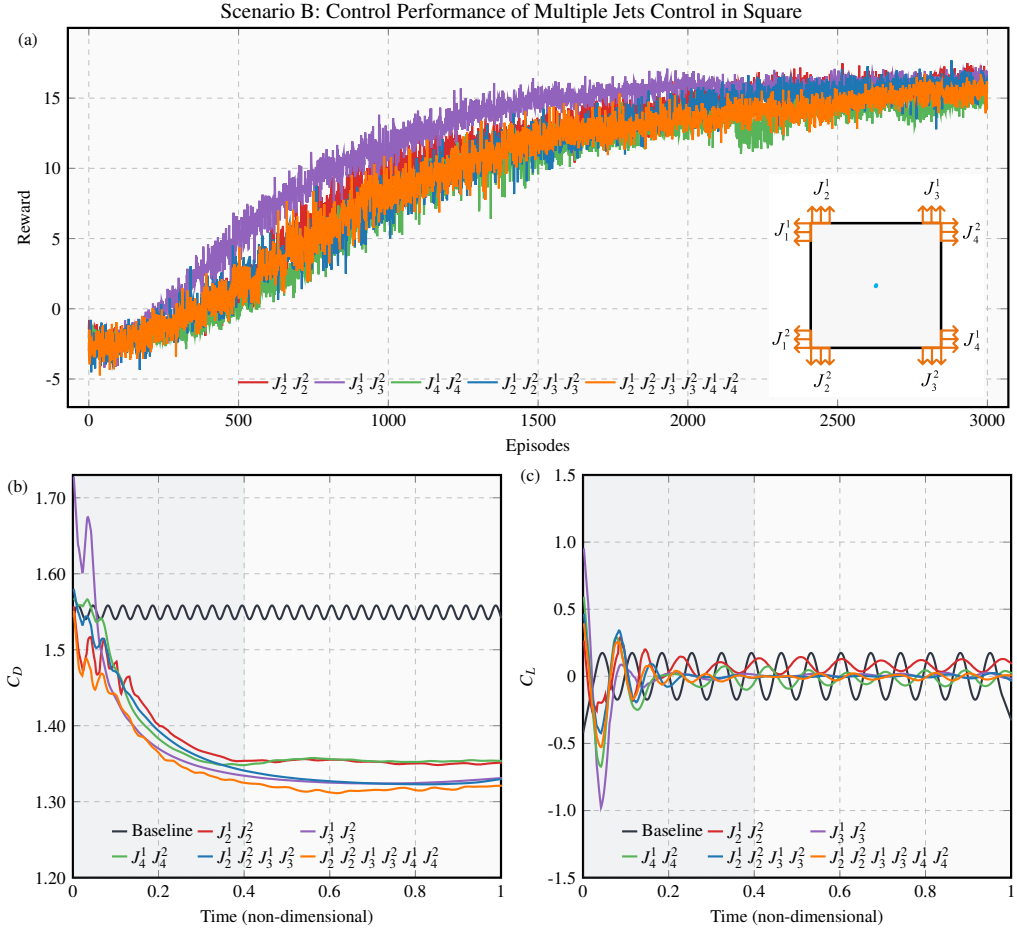


Figure 17: Evaluation of flow control performance for a square cylinder using single and multiple synthetic jets configurations. (a) Reward curves during the training process for different jet placement configurations. (b) Drag coefficient ( $C_D$ ) as a function of non-dimensional time for baseline and controlled flows. (c) Lift coefficient ( $C_L$ ) as a function of non-dimensional time for baseline and controlled flows.

effects of jet placement at the front, middle, and rear positions along the cylinder's side. Their results showed that full suppression was achieved only near the rear corners, consistent with our findings.

## 4.2. Multiple pairs of synthetic jets controllers

### 4.2.1. Scenario B: Control Performance of Multiple Jets Control

We further designed experiments to implement flow control using multiple pairs of synthetic jets simultaneously. The results of DRL training and its impact on flow control for a square cylinder with various jet configurations are illustrated in figure 17. For comparison, results using a single pair of synthetic jets are also provided. The evolution of the reward functions during training for different jet configurations is shown in figure 17(a). The reward function serves as a critical metric for evaluating the effectiveness of the DRL agent in optimizing

flow control strategies. In this figure,  $J_2^1 J_2^2$ ,  $J_3^1 J_3^2$ , and  $J_4^1 J_4^2$  represent specific jet positions on the square cylinder.

Across all four configurations, the reward functions increase as training progresses, indicating that the DRL agent is successfully learning and refining the flow control strategies. Initially, the reward values are low, reflecting the early stages of learning when the agent explores various control strategies. As the number of episodes increases, the reward function for each jet configuration shows steady improvement, particularly between 500 and 2000 episodes. The gradual rise in the reward values suggests that the DRL algorithm is progressively enhancing its strategy, leading to improved control performance. Notably, the reward function for the  $J_3^1 J_3^2$  configuration exhibits faster growth, indicating that this setup is particularly effective in achieving the control objectives. The quicker convergence suggests that the agent is learning the optimal control strategy more efficiently with this configuration. Conversely, the more gradual increase in reward functions observed when using multiple pairs of synthetic jets suggests a more incremental learning process. The slower convergence may result from increased complexity in the fluid dynamics or suboptimal jet placement for these specific control tasks.

As a function of non-dimensional time for various jet configurations, compared to a baseline scenario without active flow control, the drag coefficient is illustrated in figure 17(b). The baseline drag coefficient exhibits periodic oscillations, a typical characteristic of unsteady flow around a square cylinder without control. Upon activating the synthetic jets, the drag coefficient for all configurations decreases significantly, indicating the effectiveness of the control strategies. Specifically, the drag reduction achieved by single jet pairs positioned at  $J_2^1, J_2^2$  and  $J_4^1, J_4^2$  is less pronounced than that of the jet pair at  $J_3^1, J_3^2$ . When both  $J_2^1, J_2^2$  and  $J_3^1, J_3^2$  are activated simultaneously, the drag reduction is almost identical to that achieved by  $J_3^1, J_3^2$  alone, suggesting that adding the second jet pair ( $J_2^1, J_2^2$ ) does not provide additional benefit. However, when all three jet pairs ( $J_2^1, J_2^2, J_3^1, J_3^2$ , and  $J_4^1, J_4^2$ ) are activated together, there is a more substantial reduction in drag compared to both the single jet pair ( $J_3^1, J_3^2$ ) and the two jet pairs ( $J_2^1, J_2^2$  and  $J_3^1, J_3^2$ ). This enhanced drag reduction comes at the cost of some stability, reflecting the more complex interactions involved in controlling the flow with multiple jet pairs. This analysis highlights the trade-offs between achieving greater drag reduction and maintaining stability when using multiple synthetic jets in flow control. The results suggest that while adding more jets can further reduce drag, it may also introduce additional challenges in maintaining a stable control strategy.

Over non-dimensional time for various jet configurations, compared to a baseline scenario without active control, the lift coefficient is illustrated in figure 17(c). The baseline  $C_L$  without control exhibits periodic oscillations. The activation of synthetic jets significantly reduces both the amplitude and frequency of these oscillations, stabilizing the lift coefficient closer to zero or the desired level. This suppression of lift fluctuations helps create a more stable flow field by mitigating the unsteady forces acting on the cylinder. Specifically, the configuration with jets positioned at  $J_3^1, J_3^2$  shows a more pronounced reduction in lift compared to those at  $J_2^1, J_2^2$  or  $J_4^1, J_4^2$ . When two jet pairs ( $J_2^1, J_2^2$  and  $J_3^1, J_3^2$ ) are activated simultaneously, the reduction in lift is similar to that achieved with  $J_3^1, J_3^2$  alone, indicating that the additional jet pair does not significantly enhance control. When all three pairs of jets ( $J_2^1, J_2^2, J_3^1, J_3^2$ , and  $J_4^1, J_4^2$ ) are activated simultaneously, the oscillations in the lift coefficient become more pronounced, indicating increased flow instability. While activating all three jet pairs enhances drag reduction, it also introduces additional instability in the lift coefficient. This analysis demonstrates that the  $J_3^1, J_3^2$  configuration provides the most efficient and effective flow control, as evidenced by rapid reward function convergence, significant drag reduction, and

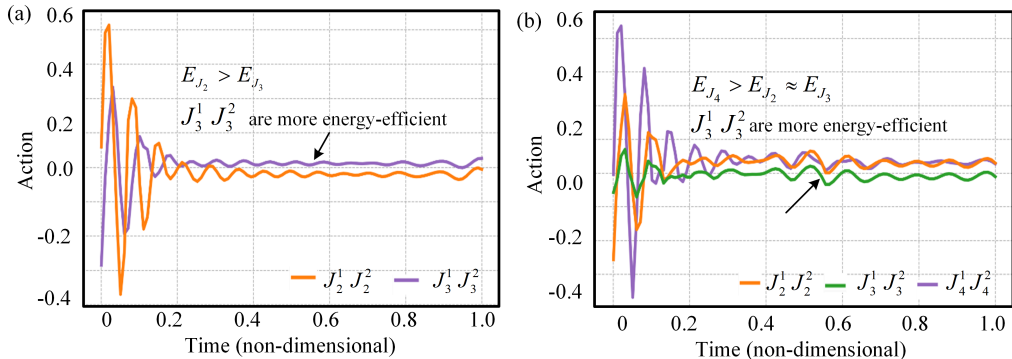


Figure 18: Comparison of energy consumption during flow control using different synthetic jets configurations around a square cylinder. (a) Energy consumption with two jet pairs  $J_2^1, J_2^2$  and  $J_3^1, J_3^2$ . (b) Energy consumption with three jet pairs  $J_2^1, J_2^2, J_3^1, J_3^2$ , and  $J_4^1, J_4^2$ .

stabilized lift. Although the simultaneous activation of two jet pairs ( $J_2^1, J_2^2$  and  $J_3^1, J_3^2$ ) yields similar control performance, it does not achieve the same level of convergence efficiency as using  $J_3^1, J_3^2$  alone. The activation of all three jet pairs, while improving drag reduction, leads to increased flow instability, which will be further analyzed in the next section in relation to the energy consumption required for flow control.

#### 4.2.2. Scenario B: Energy Consumption with Simultaneous Control (Two Pairs and Three Pairs)

The external energy consumption over non-dimensional time for flow control with two (a) and three (b) synthetic jets pairs around a square cylinder is depicted in figure 18. When comparing the single-pair synthetic jets control in figure 15 to the multi-pair configuration in figure 18, it is evident that the energy consumption in the multi-jet scenario is reduced by an order of magnitude relative to the single-jet case. Where two pairs of synthetic jets,  $J_2^1, J_2^2$  and  $J_3^1, J_3^2$ , are simultaneously employed, significant peaks in action values for both configurations are shown in the initial phase in figure 18(a), indicating a high energy demand at the onset of flow control. This peak reflects the system response to the abrupt introduction of control forces generated by the jets. As time progresses, the action values stabilize, signifying that the energy required to maintain control has reached a steady state. Notably, the energy demand for the jets positioned at  $J_3^1, J_3^2$  consistently remains lower than that for  $J_2^1, J_2^2$ , highlighting the greater energy efficiency of the  $J_3$  configuration. The sustained lower action values suggest that this configuration achieves the desired flow control with less external energy input, making it a more efficient option for long-term operation.

The control performance is illustrated in figure 18(b) when three pairs of jets ( $J_2^1, J_2^2$ ,  $J_3^1, J_3^2$ , and  $J_4^1, J_4^2$ ) are employed simultaneously. The action values indicate the energy efficiency of various jet configurations in controlling the flow around the square cylinder, with lower sustained values signifying more energy-efficient setups. Similar to the two-jet configuration, the three-jet setup also exhibits peak action values during the initial phase of control, indicative of the high initial energy demand required to establish effective control. As the system stabilizes, the action values across all jet pairs settle into a steady state. Among the three-jet configurations, the jets positioned at  $J_4^1, J_4^2$  demonstrate the highest sustained action values, indicating a higher energy requirement to maintain effective flow control. In contrast, the jets at  $J_3^1, J_3^2$  consistently show lower energy consumption compared

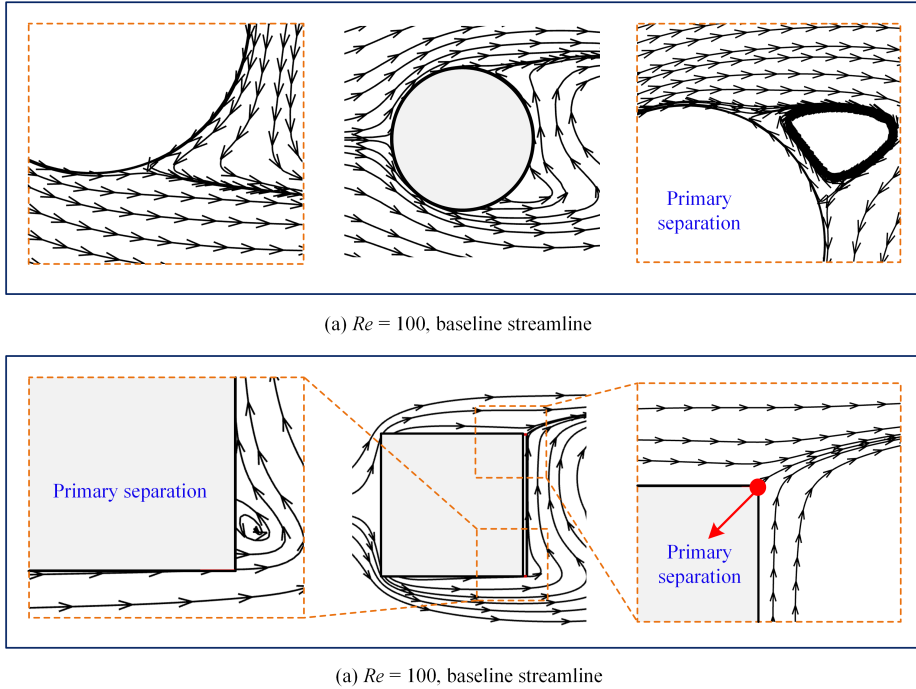


Figure 19: (a) Streamline pattern for the baseline flow at  $Re = 100$  around a circular cylinder. (b) Streamline pattern for the baseline flow at  $Re = 100$  around a square cylinder.

to those at  $J_4^1, J_4^2$  and  $J_2^1, J_2^2$ , reinforcing their observed efficiency in the two-jet scenario. The  $J_3^1, J_3^2$  configuration emerges as the most energy-efficient across both two-jet and three-jet configurations, suggesting that the jets positioned at  $J_3$  (likely near critical flow regions such as separation points) provide effective control while minimizing energy consumption. This finding aligns with conclusions drawn from single-jet scenarios, where jets at  $J_3$  consistently maintain control with minimal energy input, favoring long-term operational efficiency. The analysis underscores the importance of strategic jet placement in optimizing flow control performance while minimizing energy expenditure. The consistent performance of the  $J_3$  jets highlights their role as the optimal balance between control effectiveness and energy efficiency.

## 5. Discussion: the physical insight of flow control strategy

### 5.1. Flow separation phenomenon

§ 3 and § 4 provide a detailed examination of the effects of various jet configurations on flow control performance. To further analyze the underlying mechanisms of flow control in relation to fluid dynamics, we present a comprehensive discussion of the control performance for both circular and square cylinder flows. When  $Re = 100$ , the flow around the circular cylinder exhibits a stable laminar characteristic with well-defined separation points, as shown in figure 19. Flow separation occurs symmetrically on both sides of the cylinder, approximately  $105^\circ$  from the forward stagnation point. At this location, the adverse pressure gradient causes the boundary layer to detach from the surface, marking the onset of flow separation. This detachment initiates the formation of a wake behind the cylinder, where alternating vortices

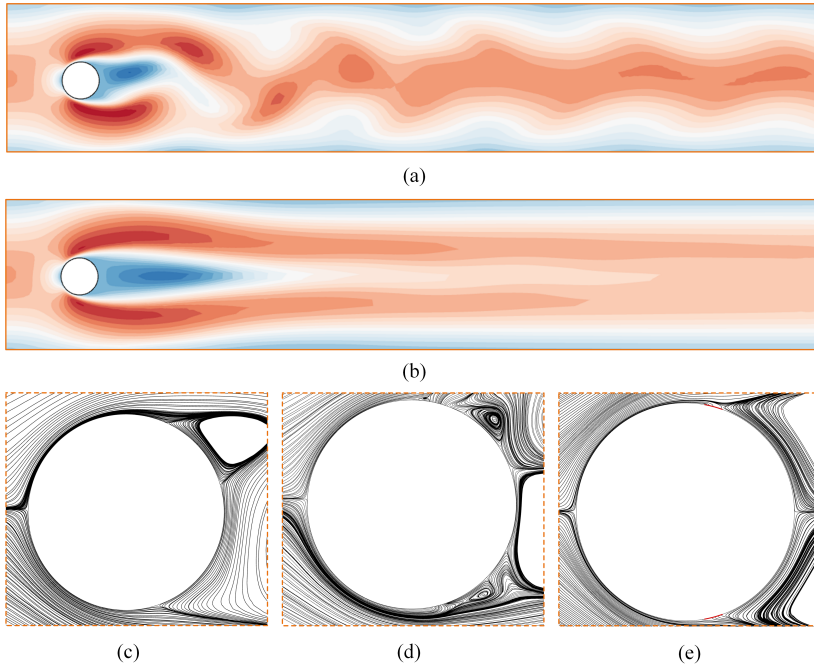


Figure 20: (a) Velocity contours of flow around a cylinder in the baseline case. (b) Velocity contours of the controlled flow with synthetic jets positioned at a  $105^\circ$  azimuthal angle. (c) Streamlines around the cylinder in the baseline case. (d) Streamlines around the cylinder with active synthetic jets at a  $105^\circ$  azimuthal angle. (e) Streamlines around the cylinder after flow control is completed with synthetic jets activated at a  $105^\circ$  azimuthal angle.

periodically shed, ultimately leading to the development of the characteristic von Kármán vortex street downstream.

In contrast, for a square cylinder at the same Reynolds number, the sharp changes in geometry result in flow separation occurring at the four sharp corners of the body. The boundary layer detaches immediately at these edges, forming distinct vortices. Especially, large separation bubbles form near the rear corners, creating a pronounced separation zone in the wake. The differing nature of flow separation around circular and square cylinders necessitates distinct control strategies, posing unique challenges when applying reinforcement learning algorithms for flow control.

### 5.2. Flow control mechanism

Through comparative analysis, the optimal position for synthetic jets around a circular cylinder is found to be at a  $105^\circ$  angle from the front stagnation point. At this position, drag and lift are significantly reduced, vortex shedding is fully suppressed, and energy consumption is minimized. This result aligns with the findings of Wang *et al.* (2024) at  $Re = 100$ , which demonstrated superior control performance using a sensor at  $105^\circ$ . Our study further confirms that the  $105^\circ$  configuration provides the best balance between energy efficiency and flow stability, as detailed in § 3. In figure 20, the flow control effectiveness of the synthetic jets positioned at  $105^\circ$  ( $J_2^1$  and  $J_2^2$ ) is illustrated, showcasing flow streamlines at three distinct time points—before, during, and after control activation. figure 20 (a) shows the baseline flow with the typical Kármán vortex street downstream of the cylinder. After activating the synthetic jets at  $105^\circ$ , the recirculation region on the cylinder’s rear side



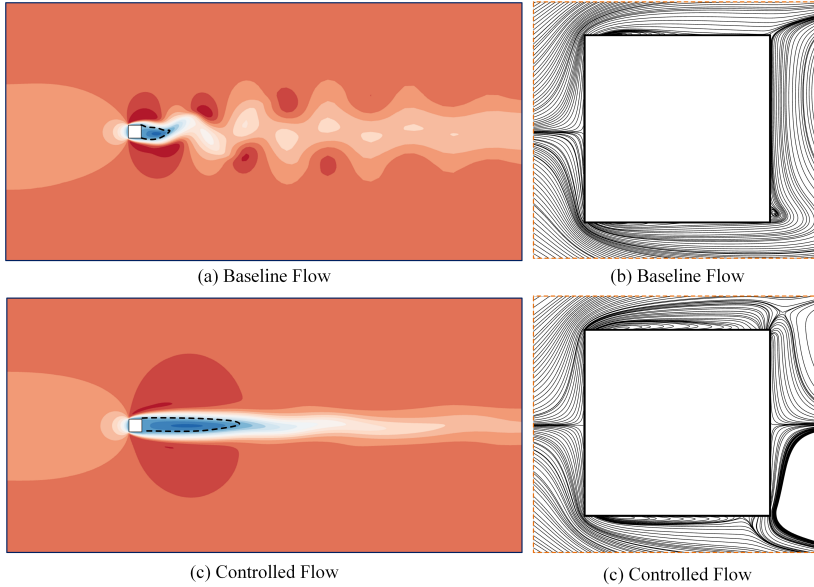


Figure 21: (a) Velocity contours of flow around a square cylinder in the baseline case. (b) Streamlines around the square cylinder in the baseline. (c) Velocity contours of the controlled flow with jets positioned at the  $J_3$  location. (d) Streamlines around the square cylinder after flow control with jets positioned at the  $J_3$  location.

expands, and vortex shedding is entirely suppressed, as depicted in figure 20 (b). And, figure 20 (c) reveals the flow separation region and the formation of a large, closed vortex on the rear side of the cylinder in baseline flow.

In figure 20 (d), when the jet positioned at the  $105^\circ$  azimuth is activated, it operates through alternating ejection and suction of the surrounding fluid, effectively altering the local flow without introducing any new mass into the system. The synthetic jets located at  $J_2^1$  and  $J_2^2$  consistently satisfy the condition  $Q_1 + Q_2 = 0$ , ensuring that the net mass flow in the system remains zero. However, the momentum and hydrodynamic impulse generated by the jets are not zero. The interaction between the synthetic jets and the crossflow leads to the formation of new vortex pairs. These high-energy vortices convect over the cylinder, locally modifying the streamlines around its surface. As a result, the apparent aerodynamic shape of the cylinder is significantly improved, along with its aerodynamic characteristics. By altering the local streamlines and inducing noticeable surface modifications, synthetic jets effectively control the flow, reducing drag and improving overall aerodynamic efficiency. [Smith & Glezer \(1998\)](#) and [Amitay et al. \(1997\)](#) experimentally demonstrated the formation, evolution, and control mechanisms of synthetic jets in flow control. Our research, utilizing a DRL-based approach, reveals a dynamically evolving flow control process that aligns with their findings. This consistency further validates the effectiveness of synthetic jets in altering flow behavior and enhancing aerodynamic performance through active flow control strategies.

In § 4, the training results for various jet configurations around the square cylinder demonstrate that positioning synthetic jets near the rear corners of the cylinder yields the optimal control performance, achieving both low energy consumption and high flow control efficiency. In this configuration, drag reduction and lift suppression are significantly enhanced, while vortex shedding in the wake is entirely suppressed with minimal external energy input. Further analysis of the separation points for both square and circular cylinders, as shown in figure 19, combined with the results from § 3 and § 4, indicates that placing

synthetic jets near the flow separation points is critical for effective flow control. Only when the jets are positioned in close proximity to these separation points can vortex shedding be fully suppressed.

In figure 21, the baseline flow is compared with the controlled flow, where jets are positioned at the rear corners ( $J_3^1$  and  $J_3^2$ ). The placement of the synthetic jets near the rear corners effectively suppresses vortex formation and stabilizes the wake flow. Streamline patterns around the square cylinder reveal significant local alterations near the rear corners due to the action of the synthetic jets. In the controlled flow, the flow separation regions on both sides of the square cylinder become more defined, and two stable, closed separation bubbles form on the cylinder’s rear face. The interaction between synthetic jets and the external flow induces significant changes in local flow patterns and streamlines, facilitating linear momentum transfer without mass addition. The alternating phases of blowing and suction generate vortices that enhance boundary layer mixing, supplying the necessary energy to overcome adverse pressure gradients and enabling complete flow reattachment around the square cylinder.

## 6. CONCLUSIONS

In this study, we employ DRL algorithms to develop and refine synthetic jet-based flow control strategies for circular and square cylinder. The primary objective is to identify optimal jet placements that achieve a balance between energy efficiency and control efficacy. A range of jet configurations, incorporating both single-action and multi-action strategies, is designed to systematically evaluate their influence on flow performance and energy consumption. Key outcomes include the identification of optimal jet positions for both circular and square cylinders, along with qualitative guidelines informed by detailed fluid dynamics analysis.

- Flow around a circular cylinder scenario. The training results indicate that when the agent is trained to control a single pair of synthetic jets, the reward function initially exhibits oscillatory increases, reflecting the agent’s exploration and learning phase, and subsequently stabilizes, indicating that the agent has progressively refined its control strategy. At positions  $J_1$  ( $120^\circ$ ) and  $J_5$  ( $60^\circ$ ), the reward function converges more slowly and to lower values, indicating these positions are less effective for training. In contrast, positions  $J_2$ ,  $J_3$ , and  $J_4$  allow for rapid convergence, suggesting better mastery of the control strategy. While all five positions achieve an 8% drag reduction and 99% suppression of the lift coefficient,  $J_1$  and  $J_5$  require more energy during the initial phase to match the performance of the other positions. When controlling a single pair of synthetic jets, the  $J_1$  ( $120^\circ$ ) and  $J_5$  ( $60^\circ$ ) positions show poor convergence and energy efficiency, making them unsuitable for optimizing flow control strategies. When training the agent to control multiple pairs of synthetic jets, multi-action control shows no significant advantage over single-action control in terms of reward function convergence, drag reduction, or lift suppression. In fact, it exhibits slightly delayed convergence and reduced lift stability. However, multi-action control proves more energy-efficient, particularly in the initial phase. When two pairs of synthetic jets are activated, energy consumption at  $J_3$  ( $90^\circ$ ) is higher than at  $J_4$  ( $75^\circ$ ) and  $J_2$  ( $105^\circ$ ), suggesting that  $90^\circ$  is not the optimal position. With three pairs of jets, the initial energy consumption is lower than with single or dual jets, and  $J_2$  ( $105^\circ$ ) offers better stability than  $J_4$  ( $75^\circ$ ). The  $J_1$  ( $120^\circ$ ) and  $J_5$  ( $60^\circ$ ) positions show poor convergence and energy efficiency, making these positions unsuitable as ideal locations for optimizing flow control strategies.

- Flow around a square cylinder scenario. When trained to control a single pair of synthetic jets, the agent performs best with jets at  $J_3$ , showing superior convergence, stability, and control performance compared to  $J_1$ ,  $J_2$ , and  $J_4$ . Jets at  $J_1$  result in the slowest convergence, poorest drag reduction, and highest instability in drag and lift coefficients, along with

increased energy consumption and fluctuations. In contrast, jets at  $J_3$  offer the most effective drag reduction, coefficient stabilization, and the lowest energy demand, making it the optimal position for control. Using two jet pairs at  $J_2$  and  $J_3$  significantly reduces and stabilizes drag and lift coefficients, with performance nearly matching that of a single jet pair at  $J_3$ . However, the reward function for the single jet pair at  $J_3$  shows faster convergence and greater stability compared to using two jet pairs, indicating higher control efficiency. Additionally, adding a third jet pair at  $J_4$  slightly improves drag reduction but decreases lift stability. When all three jet pairs ( $J_2$ ,  $J_3$ , and  $J_4$ ) are used simultaneously, the jets at  $J_3$  achieve effective flow control with minimal energy consumption. These findings suggest that the jets at  $J_3$  offer the best performance in terms of both control effectiveness and energy efficiency.

- The DRL training results reveal that, for a circular cylinder, positioning synthetic jets at an angular location of approximately  $105^\circ$  from the forward stagnation point provides the most energy-efficient control strategy while simultaneously delivering optimal flow control performance. In the case of a square cylinder, placing synthetic jets near the rear corners successfully achieves the dual objectives of minimizing energy consumption and maximizing control efficacy. Both the circular and square cylinder scenarios emphasize a pivotal finding: optimal flow control performance—defined by the complete suppression of vortex shedding, reduction in drag and lift coefficients, and enhanced flow stability—is realized when synthetic jets are strategically positioned at the flow separation points. This placement not only optimizes the effectiveness of flow control but also minimizes energy consumption, highlighting the critical importance of aligning synthetic jets positioning with key flow dynamics to achieve superior stability and efficiency in flow control performance.

The application of DRL algorithms to flow control tasks underscores the substantial potential of intelligent systems in optimizing complex flow management. The adaptive refinement of control actions in response to evolving fluid dynamics demonstrates DRL’s efficacy as a sophisticated tool in advanced fluid mechanics. This study illustrates that, through the strategic selection and positioning of jet configurations, an optimal equilibrium between energy efficiency and control effectiveness can be attained. This balance becomes especially pronounced when multiple jets are orchestrated to enhance overall flow control performance. These findings underscore the pivotal significance of strategic jet placement in attaining optimal control performance while minimizing energy expenditure.

## Appendix A. PPO algorithm

The algorithm presented below is an implementation of the proximal policy optimization with a clipped objective function. Here,  $\theta_k$  represents the policy parameters at iteration  $k$ , and  $\epsilon$  is the clipping threshold used to limit the policy update. The term  $\hat{A}_t^{\pi_k}$  denotes the estimated advantage at time step  $t$  under the current policy  $\pi_k$ . The objective function  $\mathcal{L}_{\theta_k}^{\text{CLIP}}(\theta)$  is optimized by taking  $K$  steps of stochastic gradient descent (SGD) using the Adam optimizer. The function  $r_t(\theta)$  is the probability ratio between the new and old policies, and clip limits this ratio to the range  $[1 - \epsilon, 1 + \epsilon]$ , ensuring that updates do not deviate significantly from the current policy, thereby stabilizing the training process (Schulman *et al.* 2017).

## Appendix B. Hyperparameters

The key elements and parameter settings of the PPO algorithm are described in detail in § 2.5, and table 1 provides a comprehensive summary of the hyperparameter settings used in the DRL learning algorithm.

---

**Algorithm 1** PPO with Clipped Objective
 

---

**Require:** Initial policy parameters  $\theta_0$ , clipping threshold  $\epsilon$

- 1: **for**  $k = 0, 1, 2, \dots$  **do**
- 2:   Collect set of partial trajectories  $\mathcal{D}_k$  on policy  $\pi_k = \pi(\theta_k)$
- 3:   Estimate advantages  $\hat{A}_t^{\pi_k}$  using any advantage estimation algorithm
- 4:   Compute policy update

$$\theta_{k+1} = \arg \max_{\theta} \mathcal{L}_{\theta_k}^{\text{CLIP}}(\theta)$$

by taking  $K$  steps of minibatch SGD (via Adam), where

$$\mathcal{L}_{\theta_k}^{\text{CLIP}}(\theta) = \mathbb{E}_{\tau \sim \pi_k} \left[ \sum_{t=0}^T \min \left( r_t(\theta) \hat{A}_t^{\pi_k}, \text{clip} \left( r_t(\theta), 1 - \epsilon, 1 + \epsilon \right) \hat{A}_t^{\pi_k} \right) \right]$$

5: **end for**

---

Parameter	Symbol	Value
Episode number	-	3000
Learning rate	$lr$	0.001
Discount factor	$\gamma$	0.97
Policy network	$\pi_{\theta}$	512×512
Policy Ratio Clipping	$\epsilon$	0.1
Optimizer	-	Adam
Batch size	-	120
Number of parallel environments	$n$	60

Table 1: Hyperparameters of the DRL algorithm.

---

## REFERENCES

- ALTMAN, EITAN 1999 *Constrained Markov Decision Processes*, 1st edn. Routledge.
- AMITAY, MICHAEL, HONOHAN, ANDREW, TRAUTMAN, MARK & GLEZER, ARI 1997 Modification of the aerodynamic characteristics of bluff bodies using fluidic actuators. In *28th Fluid Dynamics Conference*, p. 2004. AIAA.
- ARULKUMARAN, KAI, DEISENROTH, MARC PETER, BRUNDAGE, MILES & BHARATH, ANIL ANTHONY 2017 Deep reinforcement learning: A brief survey. *IEEE Signal Processing Magazine* **34** (6), 26–38.
- BEWLEY, THOMAS R. 2001 Flow control: new challenges for a new renaissance. *Progress in Aerospace Sciences* **37** (1), 21–58.
- BRUNTON, STEVEN L. & NOACK, BERND R. 2015a Closed-Loop Turbulence Control: Progress and Challenges. *Applied Mechanics Reviews* **67** (5), 050801.
- BRUNTON, STEVEN L. & NOACK, BERND R. 2015b Closed-Loop Turbulence Control: Progress and Challenges. *Applied Mechanics Reviews* **67** (5), 050801.
- BRUNTON, STEVEN L., NOACK, BERND R. & KOUMOUTSAKOS, PETROS 2020 Machine learning for fluid mechanics. *Annual Review of Fluid Mechanics* **52** (1), 477–508.
- CATTAFFESTA, LOUIS N. & SHEPLAK, MARK 2011 Actuators for active flow control. *Annual Review of Fluid Mechanics* **43** (1), 247–272.
- CHEN, WENJIE, WANG, QIULEI, YAN, LEI, HU, GANG & NOACK, BERND R. 2023 Deep reinforcement learning-based active flow control of vortex-induced vibration of a square cylinder. *Physics of Fluids* **35** (5), 053610.
- COLLIS, S SCOTT & JOSLIN, RONALD D 2004 Issues in active flow control: theory, control, simulation, and experiment. *Progress in aerospace sciences* **40** (4-5), 237–289.
- FAN, DIXIA, YANG, LIU, WANG, ZHICHENG, TRIANTAFYLLOU, MICHAEL S. & KARNIADAKIS, GEORGE EM

- 2020 Reinforcement learning for bluff body active flow control in experiments and simulations. *Proceedings of the National Academy of Sciences* **117** (42), 26091–26098.
- FENG, HAODONG, WANG, YUE, XIANG, HUI, JIN, ZHIYANG & FAN, DIXIA 2023 How to control hydrodynamic force on fluidic pinball via deep reinforcement learning. *Physics of Fluids* **35** (4), 045137.
- FRANÇOIS-LAVET, VINCENT, HENDERSON, PETER, ISLAM, RIASHAT, BELLEMARE, MARC G, PINEAU, JOELLE & OTHERS 2018 An introduction to deep reinforcement learning. *Foundations and Trends® in Machine Learning* **11** (3-4), 219–354.
- GLEZER, ARI & AMITAY, MICHAEL 2002 Synthetic jets. *Annual Review of Fluid Mechanics* **34** (Volume 34, 2002), 503–529.
- GRANTER, SCOTT R., BECK, ANDREW H. & PAPKE, DAVID J. 2017 Alphago, deep learning, and the future of the human microscopist. *Arch Pathol Lab Med* **141** (5), 619–621.
- GAD-EL HAK, MOHAMED 1996 Modern developments in flow control. *Applied Mechanics Reviews* **49** (7), 365–379.
- HENDERSON, PETER, ISLAM, RIASHAT, BACHMAN, PHILIP, PINEAU, JOELLE, PRECUP, DOINA & MEGER, DAVID 2018 Deep reinforcement learning that matters. In *Proceedings of the AAAI Conference on Artificial Intelligence*, , vol. 32.
- ISSA, RAAD I 1986 Solution of the implicitly discretised fluid flow equations by operator-splitting. *Journal of Computational Physics* **62** (1), 40–65.
- JAHANMIRI, MOHSEN 2010 Active flow control: a review. *Flow Measurement and Instrumentation* **21** (1), 7–28.
- JANG, DS, JETLI, R & ACHARYA, S 1986 Comparison of the piso, simpler, and simplec algorithms for the treatment of the pressure-velocity coupling in steady flow problems. *Numerical Heat Transfer* **10** (3), 209–228.
- JANIESCH, CHRISTIAN, ZSCHECH, PATRICK & HEINRICH, KAI 2021 Machine learning and deep learning. *Electronic Markets* **31**, 685–695.
- JASAK, HRVOJE, JEMCOV, ALEKSANDAR, TUKOVIC, ZELJKO & OTHERS 2007 Openfoam: A c++ library for complex physics simulations. In *International Workshop on Coupled Methods in Numerical Dynamics*, , vol. 1000, pp. 1–20.
- KAELBLING, LESLIE PACK, LITTMAN, MICHAEL L & MOORE, ANDREW W 1996 Reinforcement learning: A survey. *Journal of artificial intelligence research* **4**, 237–285.
- KAISER, LUKASZ, BABAIEZADEH, MOHAMMAD, MILOS, PIOTR, OSINSKI, BLAZEJ, CAMPBELL, ROY H, CZECHOWSKI, KONRAD, ERHAN, DUMITRU, FINN, CHELSEA, KOZAKOWSKI, PIOTR, LEVINE, SERGEY, MOHIUDDIN, AFROZ, SEPASSI, RYAN, TUCKER, GEORGE & MICHALEWSKI, HENRYK 2024 Model-based reinforcement learning for atari, arXiv: 1903.00374.
- KURZ, MARIUS, OFFENHÄUSER, PHILIPP & BECK, ANDREA 2023 Deep reinforcement learning for turbulence modeling in large eddy simulations. *International Journal of Heat and Fluid Flow* **99**, 109094.
- LECUN, YANN, BENGIO, YOSHUA & HINTON, GEOFFREY 2015 Deep learning. *Nature* **521** (7553), 436–444.
- LI, JICHAO & ZHANG, MENGQI 2022 Reinforcement-learning-based control of confined cylinder wakes with stability analyses. *Journal of Fluid Mechanics* **932**, A44, arXiv: 2111.07498.
- LI, YUXI 2018 Deep reinforcement learning: An overview, arXiv: 1701.07274.
- LIANG, ERIC, LIAW, RICHARD, NISHIHARA, ROBERT, MORITZ, PHILIPP, FOX, ROY, GOLDBERG, KEN, GONZALEZ, JOSEPH, JORDAN, MICHAEL & STOICA, ION 2018 RLlib: Abstractions for distributed reinforcement learning. In *Proceedings of the 35th International Conference on Machine Learning* (ed. Jennifer Dy & Andreas Krause), *Proceedings of Machine Learning Research*, vol. 80, pp. 3053–3062. PMLR.
- MNIH, VOLODYMYR 2013 Playing atari with deep reinforcement learning. ArXiv preprint arXiv:1312.5602, arXiv: 1312.5602.
- MNIH, VOLODYMYR, KAVUKCUOGLU, KORAY, SILVER, DAVID & OTHERS 2015 Human-level control through deep reinforcement learning. *Nature* **518** (7540), 529–533.
- NOVATI, GUIDO, DE LAROUSILHE, HUGUES L. & KOUMOUTSAKOS, PETROS 2021 Automating turbulence modelling by multi-agent reinforcement learning. *Nature Machine Intelligence* **3**, 87–96.
- PARIS, ROMAIN, BENEDDINE, SAMIR & DANDOIS, JULIEN 2021a Robust flow control and optimal sensor placement using deep reinforcement learning. *Journal of Fluid Mechanics* **913**, A25.
- PARIS, ROMAIN, BENEDDINE, SAMIR & DANDOIS, JULIEN 2021b Robust flow control and optimal sensor placement using deep reinforcement learning. *Journal of Fluid Mechanics* **913**, A25.
- PUTERMAN, MARTIN L. 1990 Chapter 8 markov decision processes. In *Stochastic Models, Handbooks in Operations Research and Management Science*, vol. 2, pp. 331–434. Elsevier.
- RABAULT, JEAN, KUCHTA, MIROSLAV, JENSEN, ATLE, RÉGLADE, ULYSSE & CERARDI, NICOLAS 2019 Artificial

- neural networks trained through deep reinforcement learning discover control strategies for active flow control. *Journal of fluid mechanics* **865**, 281–302.
- RABAULT, JEAN & KUHNLE, ALEXANDER 2019 Accelerating deep reinforcement learning strategies of flow control through a multi-environment approach. *Physics of Fluids* **31** (9), 094105.
- RABAULT, JEAN, REN, FENG, ZHANG, WEI, TANG, HUI & XU, HUI 2020 Deep reinforcement learning in fluid mechanics: A promising method for both active flow control and shape optimization. *Journal of Hydrodynamics* **32**, 234–246.
- REN, FENG, HU, HAI-BAO & TANG, HUI 2020 Active flow control using machine learning: A brief review. *Journal of Hydrodynamics* **32**, 247–253.
- REN, FENG, RABAULT, JEAN & TANG, HUI 2021 Applying deep reinforcement learning to active flow control in turbulent conditions. *Physics of Fluids* **33** (3), 037121, arXiv: 2006.10683.
- SCHÄFER, MICHAEL, TUREK, STEFAN, DURST, FRANZ, KRAUSE, EGON & RANNACHER, ROLF 1996 Benchmark computations of laminar flow around a cylinder. In *Flow Simulation with High-Performance Computers II* (ed. Ernst Heinrich Hirschel), *Notes on Numerical Fluid Mechanics (NNFM)*, vol. 48, pp. 547–566. Vieweg+Teubner Verlag.
- SCHULMAN, JOHN, LEVINE, SERGEY, ABBEEL, PIETER, JORDAN, MICHAEL & MORITZ, PHILIPP 2015 Trust region policy optimization. In *Proceedings of the 32nd International Conference on Machine Learning* (ed. Francis Bach & David Blei), *Proceedings of Machine Learning Research*, vol. 37, pp. 1889–1897. Lille, France: PMLR.
- SCHULMAN, JOHN, WOLSKI, FILIP, DHARIWAL, PRAFULLA, RADFORD, ALEC & KLIMOV, OLEG 2017 Proximal policy optimization algorithms, arXiv: 1707.06347.
- SILVER, DAVID, HUBERT, THOMAS, SCHRITTWIESER, JULIAN, ANTONOGLIOU, IOANNIS, LAI, MATTHEW, GUEZ, ARTHUR, LANCTOT, MARC, SIFRE, LAURENT, KUMARAN, DHARSHAN, GRAEPEL, THORE, LILICRAP, TIMOTHY, SIMONYAN, KAREN & HASSABIS, DEMIS 2018 A general reinforcement learning algorithm that masters chess, shogi, and go through self-play. *Science* **362**, 1140–1144.
- SILVER, DAVID, LEVER, GUY, HEESS, NICOLAS, DEGRIS, THOMAS, WIERSTRA, DAAN & RIEDMILLER, MARTIN 2014 Deterministic policy gradient algorithms. In *Proceedings of the 31st International Conference on Machine Learning* (ed. Eric P. Xing & Tony Jebara), *Proceedings of Machine Learning Research*, vol. 32, pp. 387–395. Beijing, China: PMLR.
- SMITH, BARTON L. & GLEZER, ARI 1998 The formation and evolution of synthetic jets. *Physics of Fluids* **10** (9), 2281–2297.
- SUÁREZ, P., ÁLCANTARA-ÁVILA, F., MIRÓ, A., RABAULT, J., FONT, B., LEHMKUHL, O. & VINUESA, R. 2024 Active flow control for drag reduction through multi-agent reinforcement learning on a turbulent cylinder at  $Re_D=3900$ , arXiv: 2405.17655.
- SUTTON, RICHARD S. & BARTO, ANDREW G. 2018 *Reinforcement Learning: An Introduction*, 2nd edn. Cambridge, MA: MIT Press.
- SZEPESVÁRI, CSABA & LITTMAN, MICHAEL L. 1999 A unified analysis of value-function-based reinforcement-learning algorithms. *Neural Computation* **11** (8), 2017–2060.
- TANG, HONGWEI, RABAULT, JEAN, KUHNLE, ALEXANDER, WANG, YAN & WANG, TONGGUANG 2020a Robust active flow control over a range of Reynolds numbers using an artificial neural network trained through deep reinforcement learning. *Physics of Fluids* **32** (5), 053605.
- TANG, HONGWEI, RABAULT, JEAN, KUHNLE, ALEXANDER, WANG, YAN & WANG, TONGGUANG 2020b Robust active flow control over a range of Reynolds numbers using an artificial neural network trained through deep reinforcement learning. *Physics of Fluids* **32** (5), 053605.
- VIGNON, C., RABAULT, J. & VINUESA, R. 2023 Recent advances in applying deep reinforcement learning for flow control: Perspectives and future directions. *Physics of Fluids* **35** (3), 031301.
- VIQUERAT, J., MELIGA, P., LARCHER, A. & HACHEM, E. 2022 A review on deep reinforcement learning for fluid mechanics: An update. *Physics of Fluids* **34** (11).
- VIQUERAT, JONATHAN, RABAULT, JEAN, KUHNLE, ALEXANDER, GHRAIEB, HASSAN, LARCHER, AURÉLIEN & HACHEM, ELIE 2021 Direct shape optimization through deep reinforcement learning. *Journal of Computational Physics* **428**, 110080.
- WANG, HN., LIU, N., ZHANG, YY. & OTHERS 2020 Deep reinforcement learning: a survey. *Frontiers of Information Technology & Electronic Engineering* **21**, 1726–1744.
- WANG, JIA & XU, HANG 2024a Deep reinforcement learning-based active flow control of an elliptical cylinder: Transitioning from an elliptical cylinder to a circular cylinder and a flat plate. *Physics of Fluids* **36** (7), 074117.

- WANG, JIA & XU, HANG 2024*b* Effect of synthetic jets actuator parameters on deep reinforcement learning-based flow control performance in a square cylinder. *Physics of Fluids* **36** (8), 084113.
- WANG, JIA & XU, HANG 2024*c* Optimal parallelization strategies for active flow control in deep reinforcement learning-based computational fluid dynamics. *Physics of Fluids* **36** (4), 043623.
- WANG, JIA & XU, HANG 2024*d* Robust and adaptive deep reinforcement learning for enhancing flow control around a square cylinder with varying reynolds numbers. *Physics of Fluids* **36** (5), 054103.
- WANG, Q., YAN, L., HU, G., CHEN, W., RABAULT, J. & NOACK, B.R. 2024 Dynamic feature-based deep reinforcement learning for flow control of circular cylinder with sparse surface pressure sensing. *Journal of Fluid Mechanics* **988**, A4.
- WANG, QIULEI, YAN, LEI, HU, GANG, LI, CHAO, XIAO, YIQING, XIONG, HAO, RABAULT, JEAN & NOACK, BERND R. 2022*a* DRLinFluids: An open-source Python platform of coupling deep reinforcement learning and OpenFOAM. *Physics of Fluids* **34** (8), 081801.
- WANG, YI-ZHE, MEI, YU-FEI, AUBRY, NADINE, CHEN, ZHIHUA, WU, PENG & WU, WEI-TAO 2022*b* Deep reinforcement learning based synthetic jet control on disturbed flow over airfoil. *Physics of Fluids* **34** (3), 033606.
- XIA, C., ZHANG, J., KERRIGAN, E.C. & RIGAS, G. 2024 Active flow control for bluff body drag reduction using reinforcement learning with partial measurements. *Journal of Fluid Mechanics* **981**, A17.
- YAN, LEI, LI, YUERONG, HU, GANG, CHEN, WEN-LI, ZHONG, WEI & NOACK, BERND R. 2023 Stabilizing the square cylinder wake using deep reinforcement learning for different jet locations. *Physics of Fluids* **35** (11), 115104.
- YAN, LEI, LI, YUERONG, LIU, BO & HU, GANG 2024 Aerodynamic force reduction of rectangular cylinder using deep reinforcement learning-controlled multiple jets. *Physics of Fluids* **36** (2), 025169.